





UNIVERSITY OF HAMBURG

MASTER'S THESIS

---

# **Automated Analysis of Meso-Scale Ocean-Eddies from Model Data**

---

*Author:*

NIKOLAUS KOOPMANN

*Supervisor:*

PROF. DR. CARSTEN

EDEN

2015/02/24

**TODO:abstract** will be added last...

# Contents

<b>Legend</b>	<b>7</b>
<b>1 Introduction</b>	<b>13</b>
1.1 Theory . . . . .	13
1.2 Important Papers . . . . .	19
1.3 Methods . . . . .	22
<b>2 The Algorithm</b>	<b>25</b>
2.1 Step S00: Prepare Data . . . . .	25
2.2 Step S01b: Find Mean Rossby Radii and Phase Speeds	26
2.3 Step S02: Calculate Geostrophic Parameters . . . . .	26
2.4 Step S03: Find Contours . . . . .	27
2.5 Step S04: Filter Eddies . . . . .	27
2.6 Step S05: Track Eddies . . . . .	37
2.7 Step S06: Cross Reference Old to New Indices . . . . .	39
<b>3 Results</b>	<b>41</b>
3.1 MI - 7 day time-step - AVISO . . . . .	43
3.2 MII - 7 day time-step - AVISO . . . . .	48
3.3 MII - 7 day time-step - POP . . . . .	50
3.4 MII - 7 day time-step - POP remapped to AVISO geometry . . . . .	52
3.5 MII - 1 day time-step - POP . . . . .	53
<b>4 Discussion</b>	<b>55</b>
4.1 Lengths of Tracks . . . . .	55
4.2 Scales . . . . .	56
4.3 Drift Speeds . . . . .	58
<b>Appendix A Turbulence Aspects</b>	<b>59</b>

<b>Appendix B Derivations</b>	<b>63</b>
<b>Declaration of Authorship</b>	<b>71</b>
<b>Bibliography</b>	<b>77</b>

## *Legend*

<b>Definition 1: Reynolds Number <math>Re</math></b> Compares advection of momentum to frictional acceleration. $Re = \frac{UL}{\nu}$	<b>Definition 10: Mechanical Energy per mass <math>E_k m^2/s^2</math></b> Sum of kinetic and potential Energy.
<b>Definition 2: Rossby Number <math>Ro</math></b> Compares advection of momentum to Coriolis acceleration. $Ro = \frac{U}{fL}$	<b>Definition 11: Rossby Radius <math>L_R m</math></b> The <i>geostrophic wavelength</i> . $L_R = c/f$
<b>Definition 3: Rhines Number <math>R_*</math></b> Ratio of Rhines scale to horizontal scale. $R_* = \frac{U}{\beta L^2} = \frac{a}{L} Ro$	<b>Definition 12: Steering Level <math>z_S</math></b> The critical depth where the real part of the Doppler shifted phase speed $c_S(z_S) = c(z) - u(z) = 0$ vanishes. I.e. the depth where the Doppler shift creates a standing wave, causing the disturbances to grow in place instead of spreading in space, analogous to a <i>supersonic bang</i> .
<b>Definition 4: Burger Number <math>Bu</math></b> Ratio of relative vorticity to <i>stretching</i> vorticity. $\sqrt{Bu} = \frac{NH}{fL} = \frac{L_R}{L}$	
<b>Definition 5: mass <math>m kg</math></b>	
<b>Definition 6: gravitational acceleration <math>g m/s^2</math></b> Value of surface normal component of all body forces.	
<b>Definition 7: vorticity <math>\omega_1/s</math></b>	
<b>Definition 8: Buoyancy Vector <math>B_1/s^2</math></b> $B = -\frac{\nabla \rho \times \nabla p}{\rho^2}$	
<b>Definition 9: Kinetic Energy per mass <math>E_k m^2/s^2</math></b>	

**Definition 13: Rhines Scale  $L_r$  [m]**

Scale at which earth's sphericity becomes important.

$$L_r^2 = \frac{U}{\beta} \quad (1)$$

Assuming Gaussian shape:

$$h = A e^{-(x/\sigma)^2/2}$$

$$\text{with } A = a' + a = A e^{-1/2} + a$$

$$\begin{aligned} \frac{\partial h(\sigma)}{\partial x} &= -\frac{A}{\sigma} e^{-1/2} \\ &= -\frac{a'}{\sigma} \end{aligned}$$

hence

$$\begin{aligned} L_r &= \sqrt{\frac{g}{f} \frac{\partial h}{\partial x} \beta} \\ L_r &= \sqrt{\frac{ga'}{f\sigma\beta}} \end{aligned} \quad (2)$$

**TODO:en detail:**

$$\begin{aligned} \frac{\partial h(\sigma)}{\partial x} &= -\frac{A}{\sigma} e^{-1/2} \\ &= -\frac{a}{\sigma} \frac{e^{-1/2}}{(1 - e^{-1/2})} \\ &= \frac{a}{\sigma (e^{1/2} - 1)} \end{aligned}$$

hence

$$\begin{aligned} L_r &= \sqrt{\frac{g}{f} \frac{\partial h}{\partial x} \beta} \\ L_r &= \sqrt{\frac{g}{e^{1/2} - 1} \frac{a}{f\sigma\beta}} \end{aligned} \quad (3)$$

**Definition 14: Gravity Wave Phase Speed cm/s**

$$c = \sqrt{gH}$$

**Definition 15: Reduced Gravity**

$$g'(x, y, z) \text{ m/s}^2$$

$$\text{In the layered model } g' = g \frac{\delta\rho}{\rho_0} = N^2 h$$

**Definition 16: Surface/interface Displacement  $\eta(x, y)$  m****Definition 17: Brunt Väisälä frequency**

$$N \text{ 1/s}$$

$$N^2 = g / \rho_0 \frac{\partial \rho}{\partial z}$$

**Definition 18: Mean Layer thickness  $H_m$** **Definition 19: Layer Thickness/physical height of an isopycnal surface**

$$h(x, y, t) \text{ m} / h(x, y, \rho, t) \text{ m}$$

$$h = H + \eta \text{ (in the layered model)}$$

**Definition 20: Planetary Vorticity  $\Omega$  1/s**

$$\Omega = 4\pi/\text{day}_{\text{fix}*}$$

**Definition 21: Latitude  $\phi$  rad****Definition 22: Earth's Radius  $a_m$** **Definition 23: Surface-Normal Planetary Vorticity Component  $f_1$  1/s**

$$f = f_z = \Omega \sin \phi z$$

**Definition 24: Change of Planetary Vorticity with Latitude**  $\beta_1/\text{ms}$

$$\beta = \frac{\partial f}{\partial y} = \Omega/a \cos \phi$$

**Definition 25: Okubo-Weiss Parameter**

$$O_w \text{ 1/s}^2$$

$O_w = \text{divergence}^2 + \text{stretching}^2 + \text{shear}^2 - \text{vorticity}^2.$
A negative value indicates vorticity dominated motion, whereas a positive value indicates deformation.
<b>Definition 26: Sea Surface Height SSH m</b>
<b>Definition 27: Isoperimetric Quotient IQ</b>
$IQ = A/A_c = \frac{A}{\pi r_c^2} = \frac{4\pi A}{U^2} \leq 1.$ The ratio of a ring's area to the area of a circle with equal circumference.
<b>Definition 28: Gaussian radius <math>\sigma</math> m</b>
$(H - a) = H \exp\left(-\frac{A}{2\pi\sigma^2}\right).$ Twice the Gaussian standard-deviation. $a$ : amplitude $H$ : Gaussian amplitude $A$ : determined area
<b>Definition 29: dynamic eddy scale <math>\sigma</math> m</b>
Distance from eddy's center to the line of maximum orbital speed <i>i.e.</i> the zero-vorticity contour.

<b>Definition 30: Run aviso-MI</b>
7-day time-step aviso with method MI.
<b>Definition 31: Run aviso-MII</b>
7-day time-step aviso with method MII.
<b>Definition 32: Run pop2avi-MII</b>
7-day time-step POP remapped to aviso-geometry with method MII.
<b>Definition 33: Run POP-7day-MII</b>
7-day time-step POP with method MII.
<b>Definition 34: Run POP-1day-MII-Southern-Ocean</b>
1-day time-step aviso with method MII. Southern Ocean Only. Minimum Age: 30 d Contour step raised to 2 cm
<b>Definition 35: Parallel Ocean Program (POP).</b>
Global fully non-linear $0^{\circ}6'$ , 1 d, primitive equation ocean model Oestreicher (n.d.).
<b>Definition 36: TODO:AVISO</b>
Forget (2010)



# 1

## *Introduction*

THE MAIN PURPOSE of this study is to create a computer program that is able to **detect**, **track** and **analyse** meso-scale ocean eddies via their surface signal in sea-surface-height (SSH). Due to the inherently technical character of the matter, large parts are dedicated to technicalities of the algorithm<sup>1</sup>. Oceanographic results are treated in the [results](#)- and [discussion](#)-chapters. This chapter discusses the physics of meso-scale geostrophic turbulence and introduces a handful of relevant historical papers. Since focus is on horizontal scales, translational speeds and the comparison of results between the [AVISO](#)-altimetry product and SSH-data from the [POP](#) ocean model, sections generally focus on either of these three topics.

### *1.1 Theory*

THIS section discusses the theory of meso-scale turbulence and parametrizations thereof. Geostrophic turbulence is typically characterized by rather stable, circular, coherent pressure anomalies, that rotate fluid around in a vortex in quasi-geostrophic equilibrium. These entities can persist for long periods of time in which they often travel distances on the order of hundreds of kilometers zonally. The fact that baroclinic instability leads to these vortices, instead of cascading to ever smaller scales as would be expected from chaotic turbulence, is a direct consequence of the inverse energy cascade of two-dimensional motion<sup>2</sup> (see fig. A.1.). The atmospheric analog are

<sup>1</sup> see the methods-chapter 2.

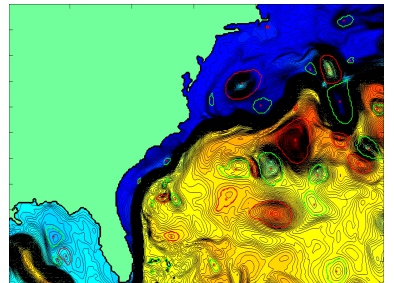


Figure 1.1: Animation snapshot of early test run. Shown is SSH with detected eddies indicated by red and green lines.

<sup>2</sup> For a discussion of this phenomenon see appendix A

storms and high-pressure systems, yet with much less difference between high- and low-pressure systems due to a smaller centrifugal force *i.e.* smaller Rossby number ( $\text{Ro}$ ). These quasi-geostrophic, meso-scale vortices, from here on called eddies<sup>3</sup>, are immediately visible on SSH-maps (see **TODO:fig of map-minus mean(SSH)**). Yet, it is difficult to physically *define* an eddy in terms of oceanographic variables. The transition from meandering jets or other undeveloped baroclinic turbulence to a coherent vortex is not very sharp. Eddies also sometimes merge or split or collectively form rifts and valleys in SSH. Detecting them on one snapshot automatically via an algorithm is therefore not trivial. Further problems arise when the algorithm is also supposed to track each individual over time. Their sheer abundance at any given time inevitably creates ambiguities as to *which is which* between time steps.

**TODO:do  $O_w$  over!**

### 1.1.1 Detection methods

- One way to find an eddy in SSH-data is to simply scan for closed contours at different values for  $z$  and then subject found entities to a series of geometric tests. Only if all criteria are met is an eddy found. This method was first used by [Chelton et al. \(2011\)](#) and is certainly a relatively simple yet very effective method, at least so for satellite data. Therefore, as a starting point, this method will be adopted and should also serve as a general definition of what will be referred to as an *eddy* hereafter<sup>4</sup>.

[Chelton et al.](#) set the following threshold criteria for his algorithm:

1. The SSH values of all of the pixels are above (below) a given SSH threshold for anticyclonic (cyclonic) eddies.
2. There are at least  $[threshold]$  pixels and fewer than  $[threshold]$  pixels comprising the connected region.
3. There is at least one local maximum (minimum) of SSH for anticyclonic (cyclonic) eddies.
4. The amplitude of the eddy is at least  $[threshold]$ .
5. The distance between any pair of points within the connected region must be less than  $[threshold]$ .

<sup>3</sup> For a discussion of the different types of vortices in the ocean see appendix ??

<sup>4</sup> The vortices will have names deviant from *eddy* where these criteria are altered.

- Another frequently used method to define an eddy makes use of the strain tensor <sup>5</sup>  $\mathbf{T}$ . The trace of the strain tensor squared includes valuable information about the dynamics of the velocity field. Namely

<sup>5</sup> see Derivation ?? 7

$$2\mathcal{O}_W = \text{Tr } \mathbf{T}^2 = \text{divergence}^2 + \text{stretching}^2 + \text{shear}^2 - \text{vorticity}^2 \quad (1.1)$$

which reduces to  $\mathcal{O}_W = (\partial_x u)^2 + 2\partial_y u \partial_x v$  in two dimensions. This is called the Okubo-Weiss-Parameter ([Okubo, 1970](#)). It is a useful tool to determine whether the field has parabolic, vorticity dominated character, or whether deformation dominates, giving hyperbolic character. An area of large negative values indicates high enstrophy density compared to gradients of kinetic energy, thus indicating little friction paired with high momentum *i.e.* a coherent, angular-momentum-conserving entity. Positive values on the other hand indicate incoherent deformation.

As ingenious as this parameter seems, it turns out that using it to identify eddies is often not the best solution. [Chelton et al. \(2011\)](#) name 3 major drawbacks:

- *No single threshold value for  $\mathcal{O}_W$  is optimal for the entire World Ocean. Setting the threshold too high can result in failure to identify small eddies, while a threshold that is too low can lead to a definition of eddies with unrealistically large areas that may encompass multiple vortices, sometimes with opposite polarities.*
- *$\mathcal{O}_W$  is highly susceptible to noise in the SSH field. Especially when velocities are calculated from geostrophy, the sea surface has effectively been differentiated twice and then squared, exacerbating small discontinuities in the data.*
- *The third problem with the W-based method is that the interiors of eddies defined by closed contours of W do not generally coincide with closed contours of SSH. The misregistration of the two fields is often quite substantial.*

It is hence only logical to scan for closed contours of SSH directly (as was done so by [Chelton et al.](#) ).

### 1.1.2 *Eddy Drift Speeds*

Intuitively any translative motion of a vortex should stem from an asymmetry of forces as in an imperfectly balanced gyroscope wobbling around and translating across a table. The main effects that cause a quasi-geostrophic ocean eddy to translate laterally can rel. easily be explained heuristically.

**Box 1. Lateral Density Gradient**

Consider a mean layer-thickness gradient  $\frac{\partial h}{\partial x} > 0$  somewhere in the high northern latitudes and a geostrophic, positive density anomaly within that layer. In other words, a high-pressure vortex or an anti-cyclonic eddy with length scale  $L \approx L_R$ . Hence a vorticity budget dominated by advection of relative vorticity and vortex stretching.

Next consider a parcel of water within the eddy's western flank. As the clockwise rotating eddy advects the parcel east via its northern side the water-column comprising said fluid will be stretched vertically as it is advected towards larger depths. In order to maintain total vorticity a small new relative-vorticity term is introduced. Since the vorticity budget is dominated by the planetary component, this new term has sign of  $f$ , i.e. positive. The net effect is that the absolute value of the parcel's (negative) relative vorticity is reduced i.e. the circular flow around the eddy's center is slowed (via term C in equation (??)), leading to an accumulation of water on the eddy's northern flank.

The opposite effect holds for a parcel advected along the southern side from east to west. Then, total (positive) vorticity is reduced so that the already negative relative vorticity becomes even more *negative*, resulting in an accelerated flow south to the eddy's core. To conserve volume the accumulation north and the decumulation of water south, the eddy is slowly pushed south.

Note that the rotational sense of the eddy is irrelevant here. In the cyclonic case, even though columns are stretched north and south directly opposite to the anti-cyclonic case, the effect on absolute values of relative vorticity is directly opposite too. I.e. vortex stretching, even though now in the south, now increases the flow, as the added term of rel. vorticity now is of the same sign as the eddy itself.

The drift direction is hence dictated by the sign of  $f$ , so that eddies in the northern hemisphere will be pushed along gradients with the shallower water always on their right and vice versa on the southern hemisphere.

**Box 2. Planetary Lift**

Assume now that  $\beta L$  be comparable or larger even than  $f_0 - \omega$  from the previous example. Then, all fluid adjacent to the eddy on its northern and southern flanks will be transported meridionally, thereby be tilted with respect to  $\Omega$  and hence acquire relative vorticity to compensate. All fluid transported north will balance the increase in planetary vorticity with a decrease in relative vorticity and vice versa for fluid transported south. This is again independent of the eddy's sense and in this case also independent of hemisphere since  $\frac{\partial f}{\partial y} = \beta > 0$  for all latitudes. The result is that small negative vortices to the northern and small positive vortices to the southern flank of eddies will push them west.

**Box 3. Eddy-Internal  $\beta$ -Effect**

In the later case clearly particles within the vortex undergo a change in planetary vorticity as well. Or from a different point of view, since  $U \sim \nabla p/f$ , and noting that the pressure gradient is the driving force here and hence fix at first approximation, particles drifting north will decelerate and those drifting south will accelerate. In order to maintain mass continuity, the center of volume will be shifted west for an anti-cyclone and east for a cyclone. Another way to look at it is to note that the only way for the discrepancy in Coriolis acceleration north and south, whilst maintaining constant eddy-relative particle speed, is to superimpose a zonal drift velocity so that net particle velocities achieve symmetric Coriolis acceleration.

**TODO:equations to follow Cushman-Roisin (1990) van Leeuwen (2007)**

### 1.1.3 The Integral Length Scale of Turbulence

1.1.3.0.1 This section is intended to shed light on the benefits of exact determinations of ocean-eddy-scales. That is, their horizontal extent *i.e.* their diameter or *wavelength*.

1.1.3.0.2 Just like the *eddy* itself, its scale is rather vague and difficult to define. What physical parameter defines the outer edge of a seamless, smooth vortex? If the eddy is detected as done by Chelton *et al.* (2011), *i.e.* closed contours of SSH the interior of which fulfilling certain criteria, the measured perimeter may jump considerably from one time step to the next. An incremental difference in the choice of  $z$  might translate to a perimeter outlining twice the difference in area, especially when SSH gradients are small.

Another possibility is to define an amplitude first, then assume a certain shape *e.g.* Gaussian, and then infer the radius indirectly. The obvious problem with this approach would be to properly define the amplitude.

The most physically sound method would have to be one depending on the eddy's most defining physical variable, that is unambiguously determinable from SSH. The geostrophic velocities. Chelton *et al.* (2011), as with everything else, tried all methods but also conclude that the later is the most adequate one.<sup>6</sup>**TODO:ref to technical chapter.**

1.1.3.0.3 Construed as an integral length scale of turbulence *i.e.* as the distance at which the auto-correlation of particles reaches zero, the *eddy-scale* turns out to be of fundamental relevance for attempts to parametrize geostrophic turbulence.

General circulation models ( $\mathcal{O}(10^2)$ km) as they are used in *e.g.* climate forecasts are too coarse to resolve meso-scale ( $\mathcal{O}(10^1)$ km) turbulence. Even if the Von-Neumann-condition were ignored and a refinement were desired horizontally only, a leap of one order of magnitude would cause an increase in calculation time of factor<sup>7</sup>  $x = 100$ . The effects of the non-linear terms therefore have to be somehow articulated in an integral sense for the large grid-boxes in the model. A common approach is to assume that *eddy kinetic energy*  $\overline{u'u'}$  and *eddy potential energy*  $\overline{w'p'}$ , akin to diffusive processes<sup>8</sup>, are

<sup>6</sup> See Chapter

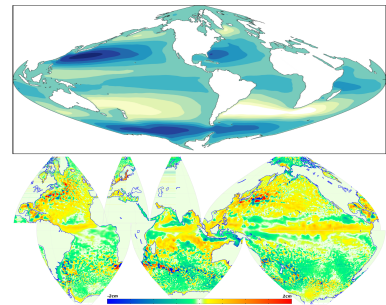


Figure 1.2: top: Stommel's equation  $F_{\text{bottom}} - F_{\text{surface}} = -v\beta$  with constant eddy viscosity. bottom: Parallel Ocean Program eddy-resolving model snapshot with SSH mean of one year subtracted.

<sup>7</sup> With the Moore's-Law-type exponential growth in FLOP/S of the last 22 years for supercomputers ( $\lg(x) \sim 3/11a$ ) a factor 100 interestingly translates to only  $a = 22/3 \approx 7$  years...

<sup>8</sup> In analogy to Fick's first law of diffusion

proportional to the gradient of  $\bar{u}$  respective  $\bar{b}$  (down-gradient-parametrization<sup>9</sup>) (Olbers *et al.*, 2012), which leads to the problem of finding expressions for the *turbulent diffusivities i.e.* the rate at which gradients are diffused by turbulence. This parameter is by no means constant, instead it can span several orders of magnitude, itself depending on the strength of turbulence-relevant gradients, and sometimes even assuming negative values (Eden & Greatbatch, 2008). Precise knowledge of the integral length scale and the physics that set it is hence vital for attempts to analyze and set values for eddy diffusivities and turbulence parametrizations in general.

<sup>9</sup> *i.e.* Reynolds averaging

## 1.2 Important Papers

### 1.2.1<sup>10</sup>

Rhines investigated the effect of the  $\beta$ -plane on the inverse energy cascade of quasi-2-dimensional atmospheric and oceanic turbulence. At constant  $f$ , energy should be cascaded to ever-larger scales until halted by the scale of the domain. This is clearly not the case, as no storm has ever grown to global scale. The presence of a meridional restoring force creates a critical scale beyond which the *turbulent migration of the dominant scale nearly ceases . . .* Instead, Rossby waves are excited which would theoretically eventually give way to alternating zonal jets of width  $L$ . This scale was later coined the Rhines Scale.

<sup>10</sup> Rhines, Peter B. 1974. Waves and turbulence on a beta-plane. *J. Fluid Mech.*, **69**(03), 417

### 1.2.2<sup>11</sup>

Bjerknes & Holmboe (1944) already noted that the  $\beta$ -effect causes a mass-imbalance in planetary vortices that, if not met by an asymmetry in shape must lead to westward propagation. Nof (1981) derived that the  $\beta$ -effect results in a net meridional force on the integrated mass of the vortex, which in balance with the Coriolis acceleration shoves cyclones eastward and anti-cyclones westward. They also explained how displaced water outside the eddy's perimeter causes a much stronger westward component, with the result that all eddies propagate westward irrespective of rotational sense. The westward

<sup>11</sup> Cushman-Roisin, B. 1990. Westward motion of mesoscale eddies. *J. Phys.* . . .

drift was also derived in various forms by *e.g.* [Flierl \(1984\)](#); [Matsuura & Yamagata \(1982\)](#).

[Cushman-Roisin \(1990\)](#) put it all into a less restricted uniform formalism by scaling the terms in the one-layer primitive equations by their respective dimensionless numbers. By integrating the interface-displacement caused by the eddy over the eddy's domain and applying mass continuity they derived for the location  $(X, Y)$  of an eddy's centroid<sup>12</sup>:

$$\begin{aligned}\Pi X_{tt} - Y_t &= L_R T \beta \langle yv \rangle + L \frac{\beta}{f} \langle y\eta v \rangle \\ \Pi Y_{tt} - X_t &= -L_R T \beta \langle yu \rangle - L \frac{\beta}{f} \langle y\eta u \rangle\end{aligned}\quad (1.2)$$

<sup>12</sup>  $\langle \cdot \rangle \equiv \frac{1}{A} \int_A dA$

where  $\Pi = 1/f_0 T$ .

Hence, independent of balance of forces the eddy's center of mass describes inertial oscillations<sup>13</sup> on the  $f$ -plane, even in the absence of  $\beta$ . Using geostrophic values for  $u$  and returning to dimensional variables equation (1.2) can be cast into:

$$X_t = \frac{\omega_{long}}{k} \left( 1 + \frac{1}{H} \frac{\int \eta^2 dA}{2V_e} \right) \quad (1.3)$$

The first term represents the ?? from [1.1.2](#), whereas the second term represents the ?. Note that the first term is always westwards, while the second has sign of  $-\eta$ , *i.e.* westward for anti-cyclones and eastward for cyclones and that the first is always larger than the second. **TODO:van Leeuwen (2007) for derivation if time**

<sup>13</sup> compare to *harmonic oscillator*

### 1.2.3 Early Altimeter Data

The advent of satellite altimetry, which Walter Munk called *the most successful ocean experiment of all time* [Orbach & Munk \(2002\)](#), finally allowed for global-scale experimental investigations of oceanic planetary phenomena on long time- and spatial scales. Among others, [Matano et al. \(1993\)](#); [Cipollini et al. \(1997\)](#); [Le Traon & Minster \(1993\)](#) were the first to use satellite-data to present evidence for the existence of Rossby waves and their westward-migration in accord with theory. Surprisingly all of the observations found the phase speeds to be 1 to 1.5 times larger than what theory predicted. Several theories to explain the discrepancy were presented. E.g. [Killworth et al.](#)

(1997) argued that the discrepancy was caused by mode-2-east-west-mean-flow velocities. Interestingly it appears that hitherto, the relevant altimeter signal was mainly associated with linear waves. Non-linearities are rarely mentioned in the papers of those years. Probably simply due to the fact that the turbulent character of much of the meso-scale variability was still obscured by the poor resolution of the first altimeter products.

#### 1.2.4 SSH Altimeter Data <sup>14</sup>

From the beginning of satellite altimetry Chelton *et al.* have invested tremendous effort to thoroughly analyze the data in terms of Rossby waves and geostrophic turbulence. At the time of the Killworth *et al.* (1997) paper only 3 years of Topex/Poseidon data alone had been available, which led them to interpret the data mainly in terms of Rossby waves. Once the merged Aviso T/P and ERS 1/2 **TODO:ref** was released 7 years later, Chelton *et al.* presented a new analysis that was based on an automated eddy-tracking algorithm using the geostrophic Okubo-Weiss parameter <sup>15,16</sup>. For the first time Satellite data was sufficiently fine resolved to unveil the dominance of *blobby (sic) structures rather than latitudinally  $\beta$ -refracted continuous crests and troughs* that had hitherto been assumed to characterize the large scale SSH picture. They presented results of a refined algorithm in their 2011 paper, in which they abandoned the Okubo-Weiss concept and instead identified eddies via closed contours of SSH itself <sup>17</sup>. Among their most significant findings is the conclusion that on the one hand, the vast majority of extra-tropical west-ward propagating SSH-variability consists of coherent, isolated, non-linear, meso-scale eddies, whilst on the other hand, these eddies propagate about 25% slower <sup>18</sup> than small amplitude features of larger lateral scale, that are difficult to separate from the data and are assumed to obey linear Rossby wave theory. **TODO:rephrase** Apart from this they find little evidence for any dispersion in the signal, neither do they find evidence for significant meridional propagation, as should be found for Rossby waves. In agreement with Rhines & Holland (1979), they find this eddy-dominated regime to fade in vicinity of the equator, giving way to the characteristic Rossby-wave profile. Almost all of their eddies propagate

<sup>14</sup> Chelton, Dudley B., Schlax, Michael G., Samelson, Roger M., & de Szoeke, Roland a. 2007. Global observations of large oceanic eddies. *Geophys. Res. Lett.*, **34**(15), L15606; and Chelton, Dudley B., Schlax, Michael G., & Samelson, Roger M. 2011. Global observations of nonlinear mesoscale eddies. *Prog. Oceanogr.*, **91**(2), 167–216

<sup>15</sup> see section 1.1.1

<sup>16</sup> see Derivation ?? 7

<sup>17</sup> note that geostrophic  $O_W$  is a second derivative of SSH and thus exacerbates noise in the SSH data.

<sup>18</sup> pointing to dispersion.

westwards. Those that are advected eastwards by *e.g.* the ACC show significantly shorter life-times than those that are not. For more detail on their results and a discussion of the limitations of eddy-tracking via satellites see section ??.

### 1.3 Methods

#### 1.3.1 Satellite vs Model Data

**1.3.1.0.4 Satellites** The latest Aviso SSH data from satellites features impressive accuracy, constancy and resolutions in both space and time. This is achieved by collecting all of the data from all of the altimeter-equipped satellites available at any given moment for any given coordinate. This conglomerate of highly inhomogeneous data is then subjected to state-of-the-art interpolation methods to produce a spatially and temporally coherent product. One satellite alone is not sufficient to adequately resolve meso-scale variability globally. Take *e.g.* the Topex/Poseidon satellite.

It had a ground repeat track orbit of 10 days and circled the earth in 112 minutes or  $\approx 13$  times a day with a swath width of 5 km. Hence it drew  $\approx 26$  5 km-wide stripes onto the globe every day. This pattern is then repeated after 10 days, which means that at the equator only  $10 \times 26 \times 5 = 1300$ km of the  $2\pi \times 6371 = 40000$ km get covered, *i.e.* 3.25%. At every 10d time step, on average, effectively  $40000/1300 - 5 = 20$ km are left blank in-between swaths on the equator. This is why, no matter how fine the resolution within the swath at one moment in time may be, the spatial resolution is so coarse.

The merged ERS-1/Topex-data as used by [Chelton et al. \(2011\)](#) has a time step of 7 days. Assuming eddy drift speeds of  $u_e = 0$  ( $10^{-1}$ )m/s implies a distance traveled per time step of  $L_{\delta t} \approx 60$ km. [Chelton et al.](#) estimate their effective spatial resolution as  $\delta x \approx 40$ km. Eddies of smaller scale are not resolved. Tracking a single eddy from one time-step to the next should hence be feasible, especially when  $u_e$  is approximately known. Problems arise when the sea level is characterized by an abundance of isolated vortices plus maybe even further meso-scale noise of comparable amplitude.

Ambiguities arise in terms of correctly matching the eddies

	POP	merged T/P - ERS-1
dx	7km – 11km	$1/3^\circ$ ( $\approx 40$ km after filtering)
dt	1d	7d
$\log_{10} 2$ filter cutoff	n/a	$2^\circ$ by $2^\circ$
z-levels	42	1
variables	SSH,S,T,u,v	SSHFacers
pot. interpolation artifacts	n/a	yes
reality	no	yes

Table 1.1: [5pt]model vs satellite data

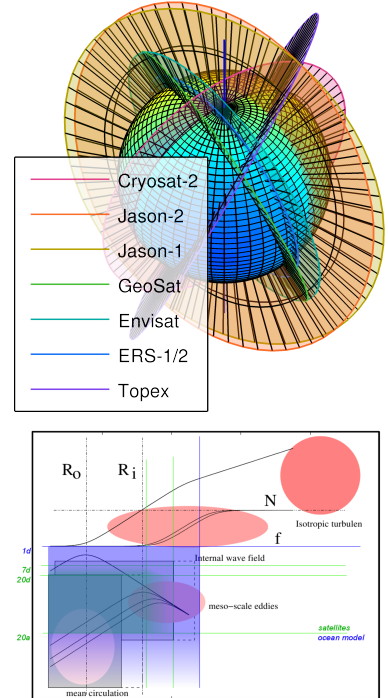


Figure 1.3: Resolutions for model vs satellite. Modified version from [Olbers et al. \(2012\)](#).

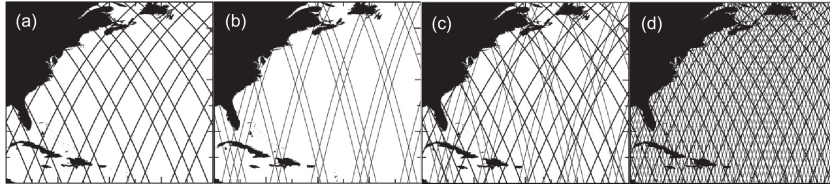
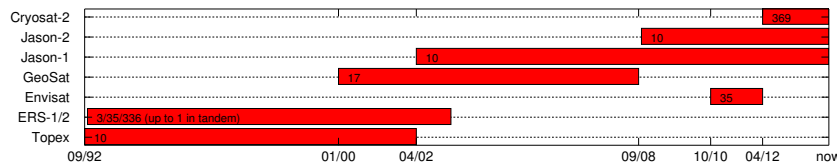


Figure 1.4: The ground track patterns for the 10-day repeat orbit of T/P and its successors Jason-1 and Jason-2 (thick lines) and the 35-day repeat orbit of ERS-1 and its successors ERS-2 and Envisat (thin lines). (a) The ground tracks of the 10-day orbit during a representative 7-day period; (b) The ground tracks of the 35-day orbit during the same representative 7-day period; (c) The combined ground tracks of the 10-day orbit and the 35-day orbit during the  $^{19}(\delta)^{10^1}$  km/day 7-day period, and (d) The combined ground tracks of the 10-day orbit and the 35-day orbit during the full 35 days of the 35-day orbit. (sic) Chelton *et al.* (2011)

from the old time-step with those in the new one, potentially causing aliasing effects in the final statistics. The translational speeds<sup>19</sup> of eddies are not really the problem here, as they usually drift slow enough to not cover more than 1 grid node per 7 day time step. The issue are those areas where eddies are born, die and merge. According to Smith & Marshall (2009) instabilities within the ACC grow at rates of up to  $1/(2\text{days})$ , which means that at a time-step up to 3 eddies have emerged and equally many died for every eddy identified within such region. The ground-repeat frequency of a satellite can of course not be set arbitrarily. Especially when the satellite is desired to cover as far north and south as possible, whilst still being subjected to just the right torque from the earth's variable gravitational field to precess at preferably a sun-synchronous frequency *i.e.*  $360^\circ/\text{year}$ . Neither can the satellite's altitude be chosen arbitrarily. If too low the oblateness of the earth creates too much eccentricity in the orbit that can no longer be frozen<sup>20</sup>. Another problem could be potential inhomogeneity in the merged data in time dimension, since products of old and current missions are lumped together into one product. This is why Chelton *et al.* (2011) opted against the finest resolution available and instead went for a product that had the most satellites merged in unison for the longest period of time.



<sup>20</sup> minimizing undulating signals in altitude by choosing the right initial values.

Figure 1.5: Length of mission. Numbers are orbit-period in days.

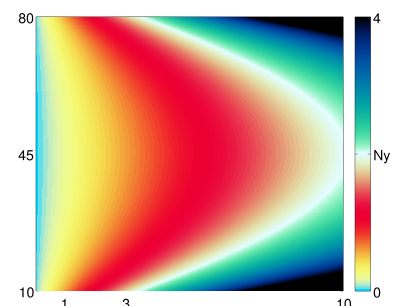


Figure 1.6:  $\xi(\phi, \mu)$ .  $Ny \equiv 2$  *i.e.* the Nyquist frequency.

**1.3.1.0.5 Ocean Model** The advantages of detecting and tracking eddies from model data are obvious. Say you have  $Bu = 1$ , so that  $L = NH/f$ . Let's assume <sup>21</sup>  $NH = a/10d$ , a model resolution of  $1^\circ/\mu$  and that the eddy diameter was twice the Rossby radius. How many grid notes  $\xi$  fit into one eddy as a function of latitude?

$$\begin{aligned}\xi \frac{a \cos \phi}{\mu} &= \frac{2NH}{f} = \frac{2NH1d}{4\pi \sin(\phi)} \\ \xi &= \frac{2\mu}{10 \sin(2\phi)}\end{aligned}\quad (1.4)$$

See figure 1.6 for the results. In this flat-bottom, constant  $\rho_z$ , Mercator-gridded model the worst eddy-resolution is interestingly at mid-latitude. A value of  $\xi > 2$  is desirable, because it eradicates ambiguities in the tracking procedure, with the result that there is no need to *forecast* the position  $x_e$  of an eddy for the new time step. It suffices to determine the closest eddy from the previous time-step for respective eddy from the new time step and vice versa. Those 2 eddies that are in agreement are successfully matched, those from the new (old) time step that do not find a match have just been born (have died). See also section **TODO:ref to section** for the technical stuff. Another major advantage of the model is that it produces not only SSH data but also all other relevant variables <sup>22</sup>, for not only the surface but for many different depths. The surface velocities inferred from altimetry are the geostrophic components only, which should suffice to *e.g.* determine the non-linearity and kinetic energy of an eddy for almost all regions, but less so for *e.g.* the western boundary currents. The *one* draw-back of using model data is that, in contrast to the satellite data, it does not represent reality. **TODO:to be continued**

<sup>21</sup> corresponds to  $L(\phi = 30^\circ) = 100\text{km}$

<sup>22</sup> See section ?? for all the possibilities that arise.

# 2

## *The Algorithm*

This section walks through the algorithm step by step, so as to explain which methods are used and how they are implemented. The idea is that the code from step S00.. on can only accept one well defined structure of data. In earlier versions the approach was to write code that would adapt to different types of data automatically. All of this extra adaptivity turned out to visually and structurally clog the code more than it did offer much of a benefit. The concept was therefore reversed. `S00_prep_data` can be altered to produce required output. Yet, there should be no need to adapt any of the later steps in any way. All input parameters are to be set in `INPUT.m` and `INPUTxxx.m`.

### *2.1 Step S00: Prepare Data*

```
function S00_prep_data
```

Before the actual eddy detection and tracking is performed, SSH-, latitude- and longitude-data is extracted from the given data at desired geo-coordinate bounds and saved as structures in the form needed by the next step (S01). This step also builds the file `window.mat` via `GetWindow3` which saves geometric information about the input and output data as well as a cross-referencing index-matrix which is used to reshape all *cuts* to the user defined geo-coordinate-geometry. The code can handle geo-coordinate input that crosses the longitudinal seam of the input data. E.g. say the input data comes in matrices that start and end on some (not necessarily strictly meridional) line straight across the Pacific and it is the Pacific only that

is to be analyzed for eddies, the output maps are stitched accordingly. In the zonally continuous case *i.e.* the full-longitude case, an *overlap* in x-direction across the *seam*-meridian of the chosen map is included so that contours across the seam can be detected and tracked across it. One effect is that eddies in proximity to the seam can get detected twice at both zonal ends of the maps. The redundant *ghost*-eddies get filtered out in S05\_track\_eddies.

## 2.2 Step S01b: Find Mean Rossby Radii and Phase Speeds

```
function S01b_BruntVaisRossby
```

This function...

- – ...calculates the pressure  $P(z, \phi)$  in order to...
  - ...calculate the Brunt-Väisälä-Frequency according to  $N^2(S, T, P, \phi) = -\frac{g(\phi)}{P} \frac{\partial \rho(S, T, P)}{\partial z}$  in order to...
- – ...integrate the Rossby-Radius  $L_R = \frac{1}{\pi f} \int_H N dz$  and ...
  - apply the long-Rossby-Wave dispersion relation to found  $L_R$  to estimate Rossby-Wave phase-speeds  $c = -\frac{\beta}{k^2 + (1/L_R)^2} \approx -\beta L_R^2$

The 3-dimensional matrices ( $S$  and  $T$ ) are cut zonally into slices which then get distributed to the threads. This allows for matrix operations for all calculations which would otherwise cause memory problems due to the immense sizes of the 3d-data<sup>1</sup>.

<sup>1</sup> E.g. the pop data has dimensions  $42 \times 3600 \times 1800$ .

## 2.3 Step S02: Calculate Geostrophic Parameters

```
function S02_infer_fields
```

This step reads the cut SSH data from S00\_prep\_data to perform 2 steps:

1. Calculate a mean over time of  $\text{SSH}(y, x)$ .
2. • use one of the files' geo-information to determine  $f, g$  and the ratio  $g/f$ .
  - calculate geostrophic fields from SSH gradients.
  - calculate deformation fields (vorticity, divergence, stretch and shear) via the fields supplied by the last step.

- calculate  $O_w$ .
- Subtract the mean from step 1 from each  $SSH(t)$  to filter out persistent  $SSH$ -gradients *e.g.* across the Gulf-Stream.

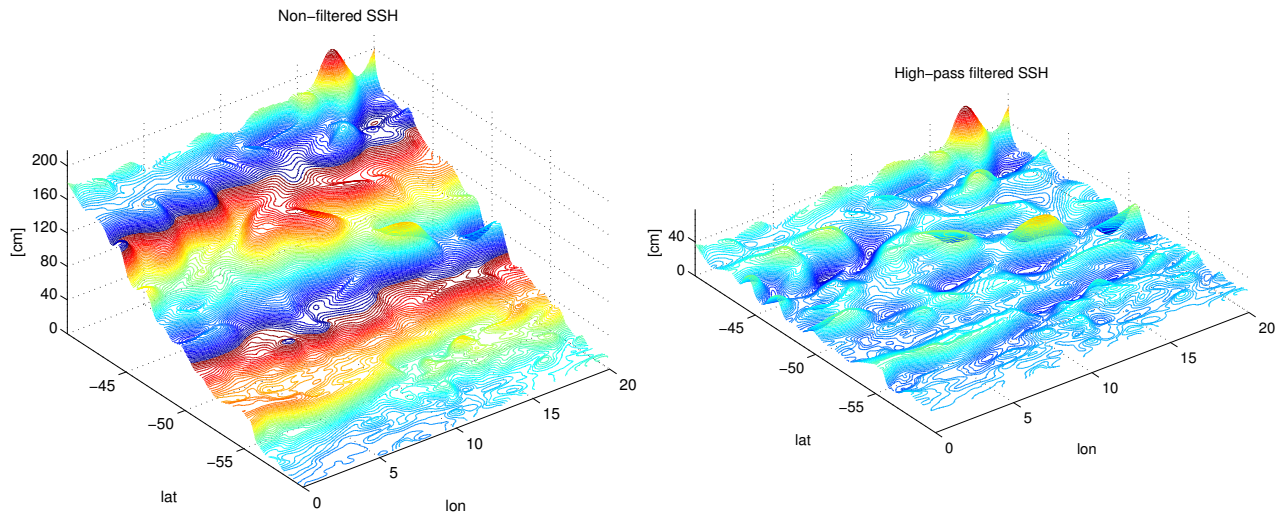


Figure 2.1:  $SSH$  with mean over time subtracted.

## 2.4 Step S03: Find Contours

```
function S03_contours
```

The sole purpose of this step is to apply MATLAB's `contourc.m` function to the  $SSH$  data. It simply saves one file per time-step with all contour indices appended into one vector<sup>2</sup>. The contour intervals are determined by the user defined increment and range from the minimum- to the maximum of given  $SSH$  data.

The function `initialise.m`, which is called at the very beginning of every step, here has the purpose of rechecking the *cuts* for consistency and correcting the time-steps accordingly (*i.e.* when files are missing). `initialise.m` also distributes the files to the threads *i.e.* parallelization is in time dimension.

<sup>2</sup> see the MATLAB documentation.

## 2.5 Step S04: Filter Eddies

```
function S04_filter_eddies
```

Since indices of all possible contour lines at chosen levels are available at this point, it is now time to subject each and every contour to a myriad of tests to decide whether it qualifies as the outline of an eddy as defined by the user input threshold parameters.

### 2.5.1 Reshape for Filtering and Correct out of Bounds Values

```
function eddies2struct
function CleanEddies
```

In the first step the potential eddies are transformed to a more sensible format, that is, a structure `Eddies(EddyCount)` where `EddyCount` is the number of all contours. The struct has fields for level, number of vertices, exact *i.e.* interpolated coordinates and rounded integer coordinates.

The interpolation of `contourc.m` sometimes creates indices that are either smaller than 0.5 or larger than  $N + 0.5$ <sup>3</sup> for contours that lie along a boundary. After rounding, this seldomly leads to indices of either 0 or  $N + 1$ . These values get set to 1 and  $N$  respectively in this step.

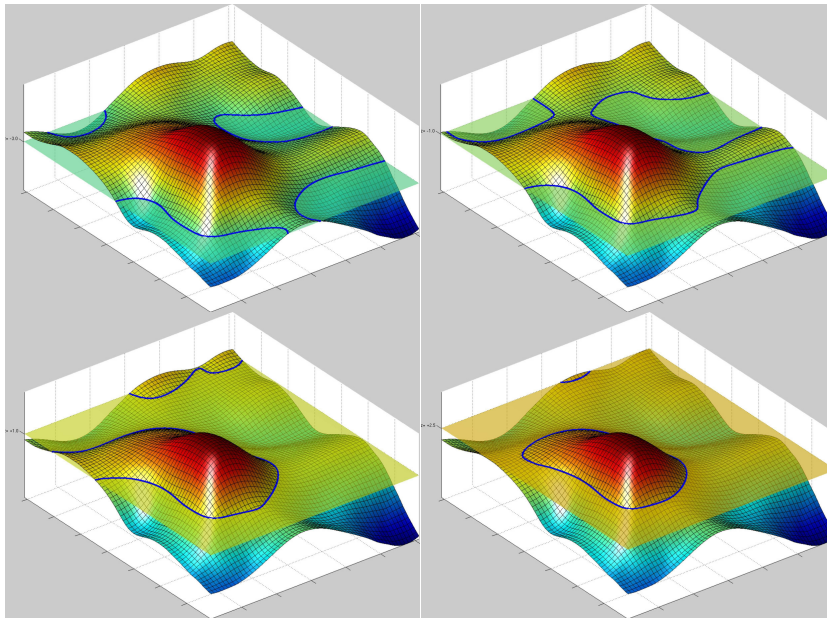
<sup>3</sup>where  $N$  is the domain size

### 2.5.2 Descent/Ascend Water Column and Apply Checks

```
function walkThroughContsVertically
```

The concept of this step is a direct adaption of the algorithm described by Chelton *et al.* (2011). It is split into two steps, one for anti-cyclones and one for cyclones. Consider *e.g.* the anti-cyclone situation. Since all geostrophic anti-cyclones are regions of relative high pressure, all anti-cyclones<sup>4</sup> effect an elevated `SSH` *i.e.* a *hill*. The algorithm ascends the full range of `SSH` levels where contours were found. Consider an approximately Gaussian shaped AC that has a peak `SSH` of say 5 increments larger than the average surrounding waters. As the algorithm approaches the sea surface from below, it will eventually run into contours that are closed onto themselves and that encompass the AC. At first these contours might be very large and encompass not only one but several ACs and likely also cyclones, but as the algorithm continues upwards found contour will get increasingly circular, describing some outer *edge* of the AC. Once the contour and its interior pass all of the tests the algorithm will decide that an AC was found and

<sup>4</sup>abbreviated AC henceforth

Figure 2.2: **TODO:YO!**

write it and all its parameters to disk. The AC's region *i.e.* the interior of the contour will be flagged from here on. Hence any inner contour further up the water column will not pass the tests. Once all AC's are found for a given time-step, the SSH flags get reset and the entire procedure is repeated only this time *descending* the SSH-range to find cyclones. The tests for cyclones and anti-cyclones are identical except for a factor  $-1$  where applicable. In the following the most important steps of the analysis are outlined.

#### **Contour filter 1 NaN-Check Contour**

```
function CR_RimNan
```

The first and most efficient test is to check whether indices of the contour are already flagged. Contours within an already found eddy get thereby rejected immediately.

#### **Contour filter 2 Closed Ring**

```
function CR_ClosedRing
```

Contours that do not close onto themselves are obviously not eligible for further testing.

#### **Contour filter 3 Sub-Window**

```
function get_window_limits, EddyCut_init
```

For further analysis a sub-domain around the eddy is cut out of the SSH data. These functions determine the indices of that window and subtract the resultant offset for the contour indices.

#### Contour filter 4 Logical Mask of Eddy Interiour

```
function EddyCut_mask
```

Basically this function creates a **flood-fill** logical mask of the eddy-interior. This is by far the most calculation intensive part of the whole filtering procedure. A lot more time was wasted on attempting to solve this problem more efficiently than time could have been saved would said attempts have been successful. The current solution is basically just MATLAB's `imfill.m`, which was also used in the very first version of 09/2013. EDIT: `imfill.m` was replaced by using `inpoly.m` to determine which indices lie within the contour-polygon. This method seems to be more exact at determining whether the inside-part of one grid cell (with respect to the smooth, spline-interpolated contour) is larger than the outside part or not.

#### Contour filter 5 Sense

```
function CR_sense
```

**All** of the interior SSH values must lie either above or below current contour level, depending on whether anti-cyclones or cyclones are sought.

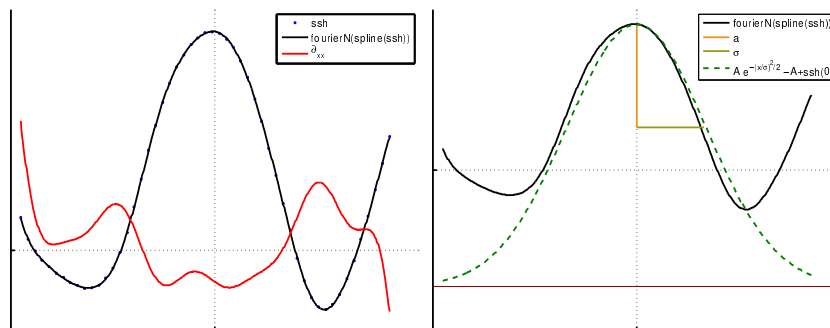


Figure 2.3: Left: Fourier-fit of an eddy from POP-SSH-data and the 2nd differential thereof. Right: Theoretical Gauss-Shape built from the resulting *standard-deviation i.e.*  $\sigma$  and amplitude.

#### Contour filter 6 Area

```
function getArea
```

The main goal here is to determine the area encompassed by the exact coordinates of the contour. It does so via MATLAB's `polyarea` function. This area is not related to the scale  $\sigma$  that is determined in 12. It is however the relevant scale for the determination of the isoperimetric quotient in 8.

If the respective switch is turned on, this function also checks that the area of found contour does not surpass a given threshold which in turn is a function of  $L_R$ . Since  $L_R$  gets very small in high latitudes a lower bound on the  $L_R$  used here should be set as well. This is especially important for the southern ocean where  $L_R$  gets very small while the strong meso-scale turbulence of the Antarctic circumpolar current results in an abundance of relatively large eddies as far south as 60°S and beyond.

### *Contour filter 7 Circumference*

```
function EddyCircumference
```

Circumference *e.g.* line-length described by the contour. This is the other parameter needed for 8. This is however neither related to the actual eddy scale determined in 12.

### *Contour filter 8 Shape*

```
function CR_Shape
```

This is the crucial part of deciding whether the object is *round enough*. A perfect vortex with  $\frac{\partial u}{\partial y} = -\frac{\partial v}{\partial x}$  is necessarily a circle. The problem is that eddies get formed, die, merge, run into obstacles, get asymmetrically advected etc. To successfully track them it is therefore necessary to allow less circle-like shapes whilst still avoiding to *e.g.* count 2 semi merged eddies as one. This is achieved by calculating the **isoperimetric quotient**, defined as the ratio of a ring's area to the area of a circle with equal circumference. Chelton *et al.* (2011) use a similar method. They require:

*The distance between any pair of points within the connected region must be less than a specified maximum Chelton *et al.* (2011).*

While this method clearly avoids overly elongated shapes it allows for stronger deformation within its distance bounds.

### *Contour filter 9 Amplitude*

```
function CR_AmpPeak
```

This function determines the amplitude *i.e.* the maximum of

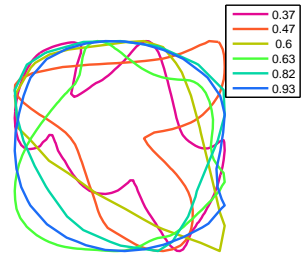


Figure 2.4: Different values of the isoperimetric quotient.

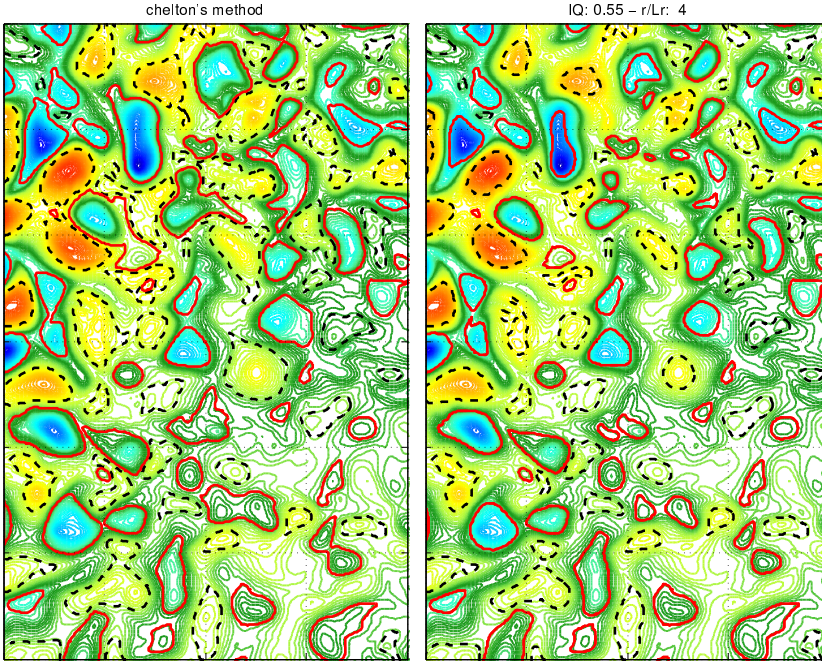


Figure 2.5: Left: The Chelton-method expects to detect eddies at their base and is rather tolerant with respect to the form of found contour. The IQ -method aims more at detecting single round vortices without expecting found contour to be necessarily related to any howsoever-defined outer edge of the eddy.

the absolute difference between SSH and current contour level and the position thereof as well as the amplitude relative to the mean SSH value of the eddy interior as done by [Chelton et al. \(2011\)](#). The amplitude is then tested against the user-given threshold. The function also creates a matrix with current contour level shifted to zero and all values outside of the eddy set to zero as well.

#### Contour filter 10 Chelton's Scales

```
function cheltStuff
Chelton et al. (2011) introduced 4 different eddy-scales.
```

1. The effective scale  $L_{\text{eff}}$  as the radius of a circle with its area equal to that enclosed by the contour.
2. The scale  $L_e$  as the radius at  $z = e^{-1}a$  with  $a$  as the amplitude with reference to the original contour and the  $z$ -axis zero-shifted to that contour. In other words the effective scale of the contour that is calculated at  $1/e$  of the original amplitude.
3. The scale  $L = L_e/\sqrt{2}$ .

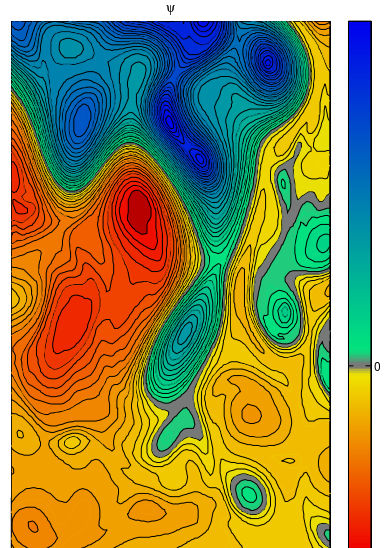


Figure 2.6: Stream function of a meandering jet shedding off a vortex. The line of strongest gradient i.e. fastest geostrophic speed later becomes the zero-vorticity-line at a theoretical distance  $\sigma$  from the center (Offset of  $\Psi$  is chosen arbitrarily).

4. The scale  $L_s$  which is *a direct estimate based on the contour of SSH within the eddy interior around which the average geostrophic speed is maximum* (Chelton et al., 2011). It is hence conceptually the same as  $\sigma$ . This scale was not calculated here, as we could not think of an efficient, simple way to estimate the area bounded by maximum geostrophic speed *i.e.* the zero-vorticity contour. To understand why this would be difficult to achieve see also sections... **TODO:ref to approp sections eg noise in vort etc.**

### Contour filter 11 Profiles

```
function EddyProfiles
```

This step

- saves the meridional and zonal profiles of SSH, U and V through the eddy's peak and spanning the entire sub-domain as described in 4.
- creates spline functions from the ssh-profiles and uses them to interpolate the profiles onto 100-piece equi-distant coordinate vectors to build smooth interpolated versions of ssh-profiles in both directions.
- in turn uses the splined data to create smooth 4-term Fourier-series functions for the profiles.

### Contour filter 12 Dynamic Scale ( $\sigma$ )

```
function EddyRadiusFromUV
```

The contour line that is being used to detect the eddy is not necessarily a good measure of the eddy's *scale i.e.* it doesn't necessarily represent the eddy's outline very well. This becomes very obvious when the area, as inferred by 6, is plotted over time for an already successfully tracked eddy. The result is not a smooth curve at all. This is so because at different time steps the eddy usually gets detected at different contour levels. Since its surrounding continuously changes and since the eddy complies with the testing-criteria the better the closer the algorithm gets to the eddy's peak value, the determined area of the contour jumps considerably between time steps. This is especially so for large flat eddies with amplitudes on the order of 1cm. If the contour increment is on that scale as



Figure 2.7: Zonal x- and z-normalized cyclone-profiles (early data ~ '13/12).

well, the difference in contour-area between two time steps easily surpasses 100% and more. Since there is no definition for the *edge* of an eddy, it is defined here as the ellipse resulting from the meridional (zonal) diameters that are the distances between the first local extrema of orbital velocity (one negative, one positive) away from the eddy's peak in y- (x-) directions<sup>5</sup>. In the case of a meandering jet with a maximum flow speed at its center, that is shedding off an eddy, this scale corresponds to half the distance between two opposing center-points of the meander. It is also the distance at which a change in vorticity-polarity occurs and is thus assumed to be the most plausible dividing line between vortices.

Trying to determine the location where this sign change in vorticity occurs in the profiles turns out to be very tricky. What we seek are local extrema of the geostrophic speeds *i.e.* of the ssh-gradients  $h_x$ . In a perfect Gaussian-shaped eddy, these would simply correspond to the first local extrema of  $h_x$  away from the peak. In *reality* the eddies can be very wobbly with numerous local maxima and minima in the gradients of their flanks. One could argue, that it must be the largest extrema, as it is the highest geostrophic speeds that are sought. In practice<sup>6</sup> multiple superimposed signals of different scales often create very strong gradients locally. But the main issue here is that one weak eddy adjacent to one strong eddy also has the stronger gradients of the stronger one within its domain so that simply looking for the fastest flow speeds along the profiles is insufficient. It is also not possible to restrict the cut domain to the extent of a single eddy only, because at the point where the domain is selected, we do not know yet whether the detection algorithm *took bait* at the eddy's base or later close to the tip.

The best method thus far seems to be to use the Fourier-series functions from 11 to determine the first extrema away from the eddy's peak. The Fourier order was chosen to be 4 by trial and error. The effect is that small-scale low-amplitude noise is avoided, allowing for more reliable determinations of  $\nabla^2 h_{\text{four}} = 0$

Once the zero crossings in all 4 directions are found, their mean is taken as the eddy's scale.

<sup>5</sup>The velocities are calculated from the gradients of 4th-order Fourier fits to the SSH profile in respective direction (see [TODO:ref](#)).

<sup>6</sup>especially for the high-resolution model data.

### Contour filter 13 **Dynamic Amplitude**

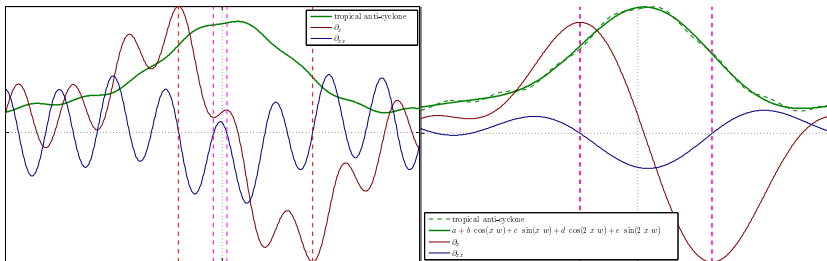


Figure 2.8: A flat wobbly low-latitude eddy resulting in multiple zero-crossings of its  $\nabla^2$ . The problem is addressed by differentiating the profile's Fourier-Series fit instead.

```
function EddyAmp2Ellipse
```

As mentioned above, the contour that helps to detect the eddy is not representative of its extent. This is also true for the  $z$ -direction, for the same reasons. This function therefore takes an SSH-mean at indices of the ellipse created by the determined zonal and meridional *dynamical* diameters, and uses this as the basal value to determine a *dynamic* amplitude.

### Contour filter 14 Center of Volume (CoV)

```
function CenterOfVolume
```

Instead of using the geo-position of the eddy's peak in the tracking procedure, it was decided to instead use the center of the volume created by the basal shifted matrix from 9 i.e. *the center of volume of the dome (resp. valley) created by capping off the eddy at the contour level*. This method was chosen because from looking at animations of the tracking procedure it became apparent that, still using peaks as reference points, the eddy sometimes jumped considerably from one time step to the next if two local maxima existed within the eddy. E.g. in one time-step local maximum A might be just a little bit larger than local maximum B and one time-step later a slight shift of mass pushes local maximum B in pole position, creating a substantial jump in the eddy-identifying geo-position hence complicating the tracking procedure.

### Contour filter 15 Geo Projection

```
function ProjectedLocations
```

An optional threshold on the distance an eddy is allowed to travel over one time-step is implemented in the tracking algorithm 2.5. This is a direct adaptation of the ellipse-based constraint described by Chelton *et al.* (2011). The maximum

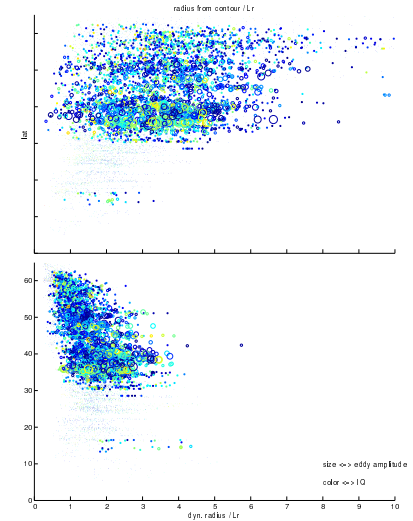


Figure 2.9: Eddies in the North-Atlantic. Y-axis: latitude. X-axis top: ratio of radius of circle with equal area to that of found contour to local Rossby-radius. X-axis bottom: ratio of  $\sigma$  to local Rossby-radius. Color-axis: Isoperimetric Quotient. Size: amplitude. The bottom plot suggests that a ratio of say 4 for  $\sigma / L_R$  should be a reasonable threshold. Same graph for the Southern Ocean looks very different though (not shown here), in that said ratio often exceeds ratios as high as 10 and larger in the far south where  $L_R$  becomes very small. This problem was addressed by prescribing a minimum value  $L_R = 20\text{ km}$  for the calculation of the scale-threshold.

distance in western direction traveled by the eddy within one time-step is limited according to  $x_{\text{west}} = \alpha c \delta t$  with  $c$  as the local long-Rossby-wave phase-speed and

*e.g.*  $\alpha = 1.75$ . In eastern direction the maximum is fixed to a value of *e.g.*  $x_{\text{east}} = 150\text{km}$ . This value is also used to put a lower bound on  $x_{\text{west}}$  and for half the minor axis ( $y$ -direction) of the resultant ellipse.

This function builds a mask of eligible geo-coordinates with respect to the next time-step.

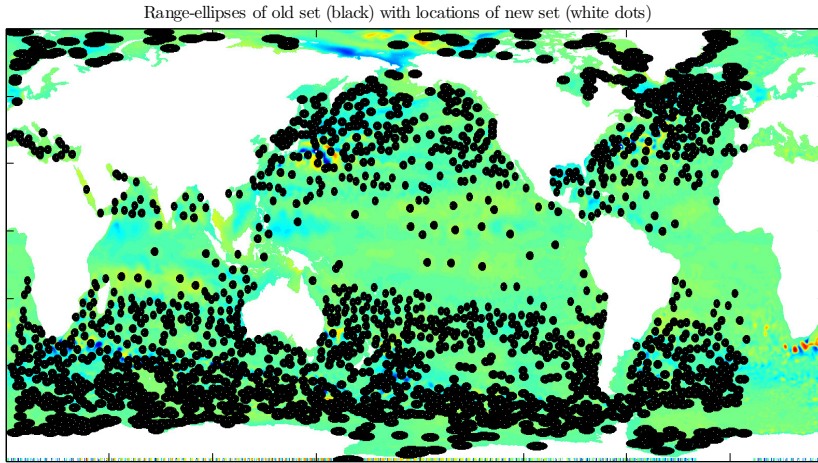


Figure 2.10: Among the saved meta-information for each eddy are also the indices describing the ellipse that defines the eddy's allowed locations with respect to the next time-step.

## 2.6 Step S05: Track Eddies

S05\_track\_eddies

### 2.6.1 Main Tracking Procedure

Due to the relatively fine temporal resolution (daily) of the model data, the tracking procedure for this case turns out to be much simpler than the one described by Chelton *et al.* (2007). There is almost no need to project the new position of an eddy, as it generally does not travel further than its own scale in one day. This means that one eddy can usually<sup>7</sup> be tracked unambiguously from one time step to the next as long both time-steps agree on which eddy from the *other* time-step is located the least distance away. The algorithm therefor simply builds an arc-length-distance matrix between all old and all new eddies and then determines the minima of that matrix in both directions *i.e.* one array for the new with respect to the old, and one for the old with respect to the new set. This leads to the following possible situations:

- Old and new agree on a pair. *I.e.* old eddy  $O_a$  has a closest neighbour  $N_a$  in the new set and  $N_a$  agrees that  $O_a$  is the closest eddy from the old set. Hence the eddy is tracked.  $N_a$  is  $O_a$  at a later time.
- $N_a$  claims  $O_a$  to be the closest, but  $N_b$  makes the same claim. *I.e.* two eddies from the new set claim one eddy from the old set to be the closest. In this situation the closer one is decided to be the old one at a later time-step and the other one must be a newly formed eddy.
- At this point all new eddies are either allocated to their respective old eddies or assumed to be *newly born*. The only eddies that have not been taken care of are those from the old set, that *lost* ambiguity claims to another old eddy, that was closer to the same claimed new eddy. *I.e.* there is no respective new eddy available which must mean that the eddy just *died*. In this case the entire track with all the information for each time step is archived as long as the track-length meets the threshold criterium. If it doesn't, the track is abandoned.

<sup>7</sup>The only exception being the situation when one eddy fades and another emerges simultaneously and in sufficient proximity.

### 2.6.2 Improvements

The former is the core of the tracking algorithm. It is almost sufficient by itself as long as the temporal resolution is fine enough. The larger the time-step, the more ambiguities arise, which are attempted to be mitigated by flagging elements of the distance matrix not meeting certain thresholds:

- `function checkDynamicIdentity`

Consider the ambiguous case when there are two eddies  $N_a$  and  $N_b$  in sufficient proximity to eddy  $O_a$ . Let's assume  $O_a$  is a relatively solid eddy of rel. large scale with a steep slope *i.e.* large amplitude and that  $N_a$  is merely a subtle blob of an eddy whilst  $N_b$  is somewhat similar to  $O_a$  but with only half the amplitude. The situation then is clear:  $N_b$  is the, apparently slowly dying,  $O_a$  at a later time, while  $N_a$  could either be a newly formed eddy, an old eddy with its respective representation in the old set something other than  $O_a$ , or even just temporary coincidental noise not representative of any significant meso-scale vortex. This interpretation should hold even when  $O_a$  sat right between the other two, thereby being much closer to  $O_a$  than  $N_b$  was.

The purpose of this step is to make such decisions. It does so by comparing the *dynamic* versions of amplitude and scale (`ampToEllipse` and  $\sigma$ ) between the time-steps. If either ratio from new to old<sup>8</sup> surpasses a given threshold the pair is flagged as non-eligible. It is important to use the *dynamic* parameters rather than those stemming from the contour line, because as mentioned in 12 the contour line itself and the eddy's geometric *character* are hardly correlated at all. One eddy can get detected at different z-levels from one time-step to the next, resulting in completely different amplitudes, scales and shapes with respect to the contour.

The initial idea was, by assuming Gaussian shapes, to construct a single dimensionless number representing an eddy's geometrical character built upon the contour-related amplitude- and scale values only. Since we have no information about the vertical position of a given contour with respect to assumed Gauss bell, this problem turned out to be intrinsically under-determined and hence useless. The method eventually used, which checks amplitude and scale

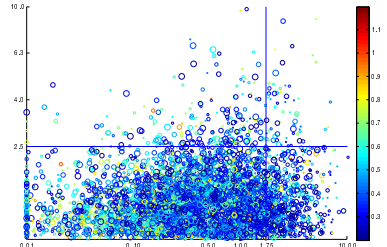


Figure 2.11: Each circle represents one eddy in the new time step. Y-axis: Maximum ratio to closest eddy in old set of either amplitude or  $\sigma$ , where 1 means *identical* and 2 means factor 2 difference. The threshold used for the final runs was 2. X-axis: Ratio of distance to closest eddy from old set divided by  $\delta t$  to local long-Rossby-wave phase-speed. Color-axis: Isoperimetric Quotient. Radius of circles: ratio of  $\sigma$  to local Rossby-radius. All eddies with said ratio larger than 10 are omitted. Note the obvious inverse correlation of scale to IQ, suggesting that all large eddies likely represent more than one vortex.

<sup>8</sup> In order to compare in both directions equally:  $\exp(|\log(v_n/v_o)|)$  where  $v$  is either amplitude or scale.

separately is again very similar to that described by Chelton *et al.* (see Box 4).

- `function nanOutOfBounds`

This is the second half to the prognostic procedure described in 2.6. It simply flags all pairs of the distance matrix for which the index representing the *new* eddy's geographic location is not among the set of indices describing the ellipse<sup>9</sup> around respective *old* eddy.

<sup>9</sup> see figure 2.10.

- `function checkAmpAreaBounds`

**TODO:relevant only for chelton method!**

## 2.7 Step S06: Cross Reference Old to New Indices

```
function S05_init_output_maps
```

The output Mercator-maps usually have different geometry from the input maps'. This step allocates all grid nodes of the input data to their respective nodes in the output map. Each output cell will then represent a mean (or median or std) of all input-nodes falling into that square.

### 2.7.1 Running the Code

The separate steps can be run all at once via `Sall.m` or one by one, as long as they are started consecutively in the order indicated by their name (`s00..`, then `s01.. ifnextchar.etcetc.`). `s01b` is not necessary though. Each step saves its own files which are then read by the next step. All output data is saved in the user given root-path from `??`. This concept uses quite a lot of disk space and is also quite substantially slowed by all the reading and writing procedures. The benefits, on the other hand, are that debugging becomes much easier. If the code fails at some step, at least all the calculations up to that step are dealt with and do not need to be re-run. The concept also makes it easy to extend the code by further add-ons.

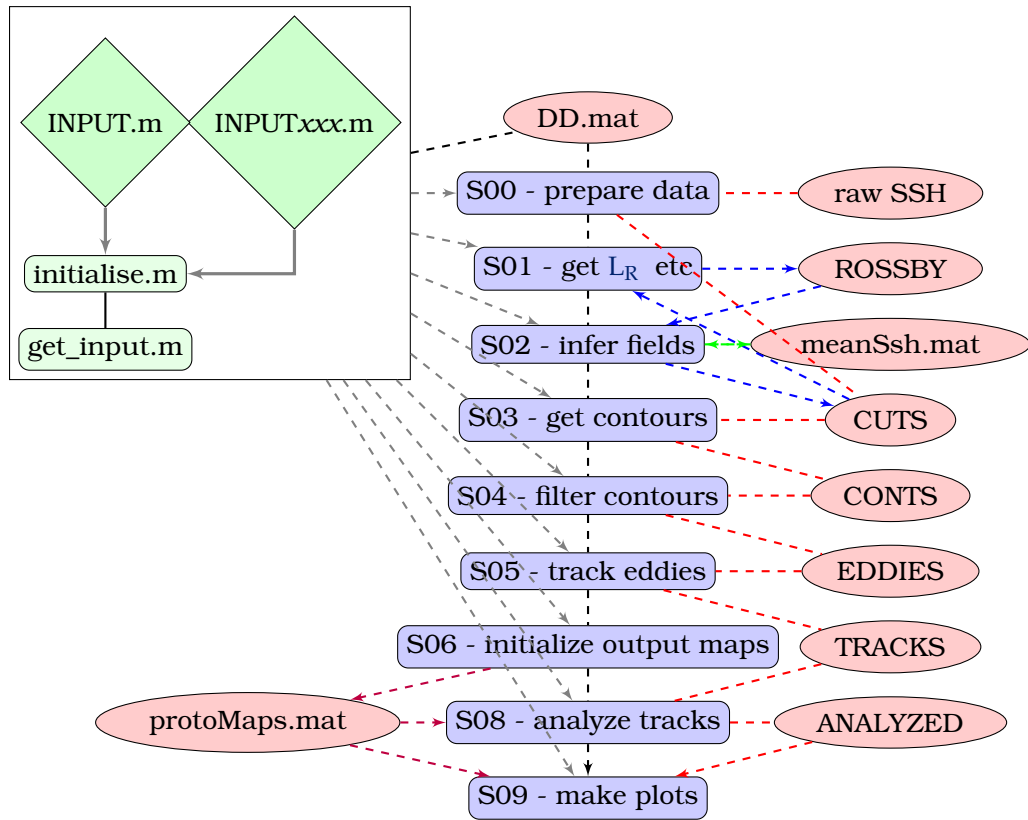


Figure 2.12: Basic code structure. The only files that are to be edited are the INPUT files. INPUT.m is independant of the origin of data, whilst the files INPUTAviso.m, INPUTpop.m etc set source-specific parameters. Each of the SXx-steps initially calls initialise.m, which in turn scans all available data, reads in the INPUT data via get\_input.m, corrects for missing data etc and creates DD.mat. The latter is the main meta-data file, which gets updated throughout all steps. All data is built step-by-step along the consecutive SXx-steps (red line). The SXx-steps are the only programs that have to be called (in order) by the user. Missing data is filled automatically in each step (Note that meanSsh.mat should be recalculated if the time span is changed!).

# 3

## Results

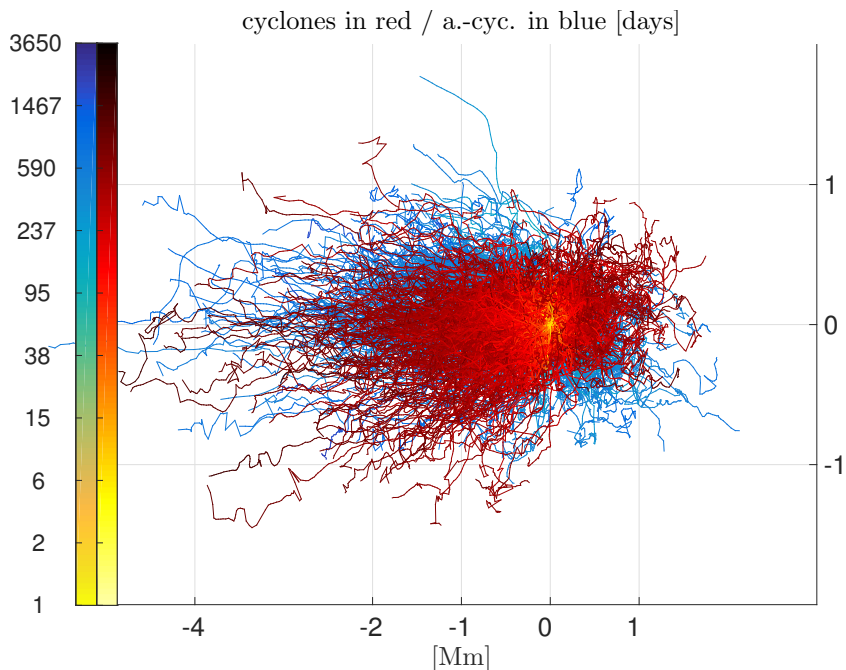


Figure 3.1: aviso-MI: Baseline-shifted *old* tracks. Tracks younger than 500 days omitted.

The short time-frame and limited computational resources allowed for only a few complete global runs over the available data. It was therefore critical to carefully choose which methods/parameters to use in order to maximize the deducible insight from the results. For best comparability of the results with each other it was decided to agree on one complete set of parameters as a basis, which would then be altered at key param-

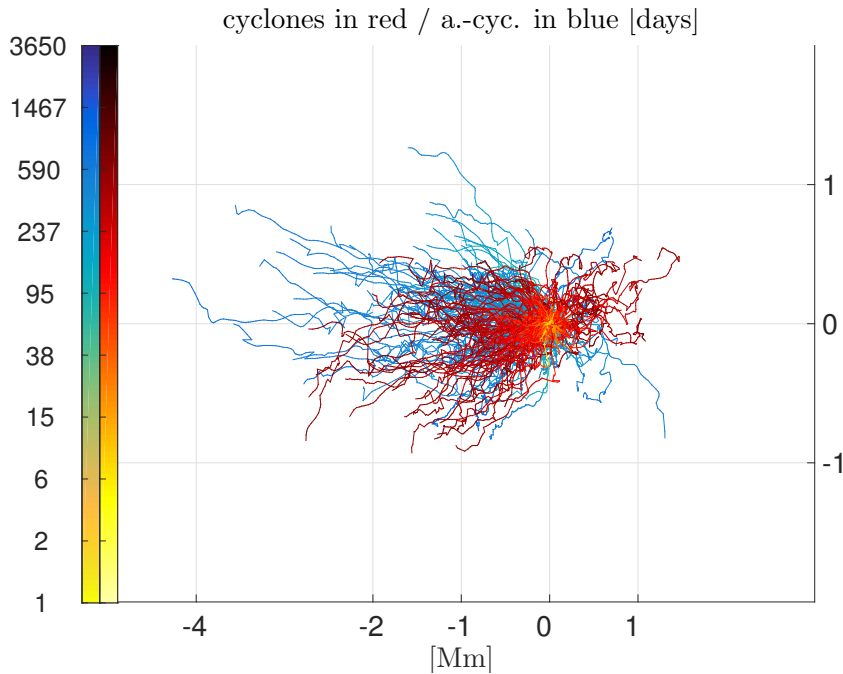


Figure 3.2: aviso-MII: Baseline-shifted *old* tracks. Tracks younger than 500 days omitted.

eters. The first run is an attempt to reproduce the results from Chelton *et al.* (2011), by setting the algorithm to be the most similar to the algorithm described by ([alias?](#)). The SSH-data for this run is therefor that of the Aviso product. This method will be called **MII**.

The second run is equivalent, except that this time the alternative **IQ**-based shape filtering method from TODO ref and the slightly different tracking-filter as described in TODO ref are used. This setting will be called **MII**. **MII** is then fed with 7-day time-step POP data as well.

To investigate what role space-resolution plays, the POP data was remapped to that of the Aviso data and fed to the **MI** method. Finally, to investigate the effects of resolution in time, an **MII**/3-day-time-step run over POP data was executed.

Start and end dates were fix for all runs as the intersection of availability of both data sets (see table 3.1 for details).

TODO lookup term used for krummes grid  
TODO check tables for completeness

**TODO:Cheltons idendity check takes Leff?**

time frame	1994/01/05 till 2006/12/27
scope	full globe (80S : 80N 180W : 180E)
AVISO geometry	641x1440 true Mercator
POP geometry	2400x3600
contour step	0.01
<b>thresholds</b>	[all SI]
max $\sigma/L_R$	4
min $L_R$ TODO	20e3
min <b>IQ</b>	0.55
min data points of an eddy	8
max(abs(rossby phase speed)) TODO	0.2
max amplitude TODO	0.01

Table 3.1: Fix parameters for all runs.

**Box 4. Method MI**

The concepts used in this method are mostly based on the description of the algorithm described by Chelton *et al.* (2011) and all parameters are set accordingly. Basically MI is a modification of MII (which was completed first), with the aim to try to recreate the results from (Chelton *et al.*, 2011). It differs from MII in the following:

• **detection**

As mentioned in TODO ref, the approach by Chelton *et al.* (2011) is to avoid overly elongated objects by demanding:

- high latitudes  
The maximum distance between any vertices of the contour must not be larger than 400km for  $|\phi| > 25^\circ$ .
- low latitudes  
The 400m-threshold increases linearly towards the equator to 1200m.

• **tracking**

The other minor difference to MII is in the way the tracking algorithm flags eddy-pairs between time-steps as sufficiently similar to be considered successful tracking-candidates (see TODO ref). In this method an eddy B from time-step  $k+1$  is considered as a potential manifestations of an eddy A from time-step  $k$  as long as both - the ratio of amplitudes (with regard to the mean of SSH within the found contour) and the ratio of areas (interpolated versions as discussed in TODO ref) fall within a lower and an upper bound.

**Box 5. Method MII**

Even though, in its core, directly inspired by Chelton *et al.* (2011), this method differs from MII and thus from the description by Chelton *et al.* mainly in the way the shape of a found contour is deemed sufficiently eddy-like.

• **detection**

The IQ -method. See 2.5 and 8.

• **tracking**

Conceptually similar to MI, it is again vertical and horizontal scales that are compared between time-steps. Preferring a single threshold-value over one upper and one lower bound, a parameter  $\xi$  was introduced that is the maximum of the two values resulting from the two ratios of amplitude respective  $\sigma$ , where either ratio is -if larger- its reciprocal in order to equally weight a decrease or an increase in respective parameter. In other words:  $\xi = \max(|\exp|\log R_\alpha|; |\exp|\log R_\sigma||)$ , where  $R$  are the ratios.

### 3.1 MI - 7 day time-step - AVISO

THE RESULTS from the MI-method are special in that they feature many long-lived eddies (see Figures 3.1, 3.3 and 3.5), some of which travelled more than 4000 km west. Tracks were recorded throughout the entire world ocean with the only exceptions being an approximately 20°-wide stripe along the equator.

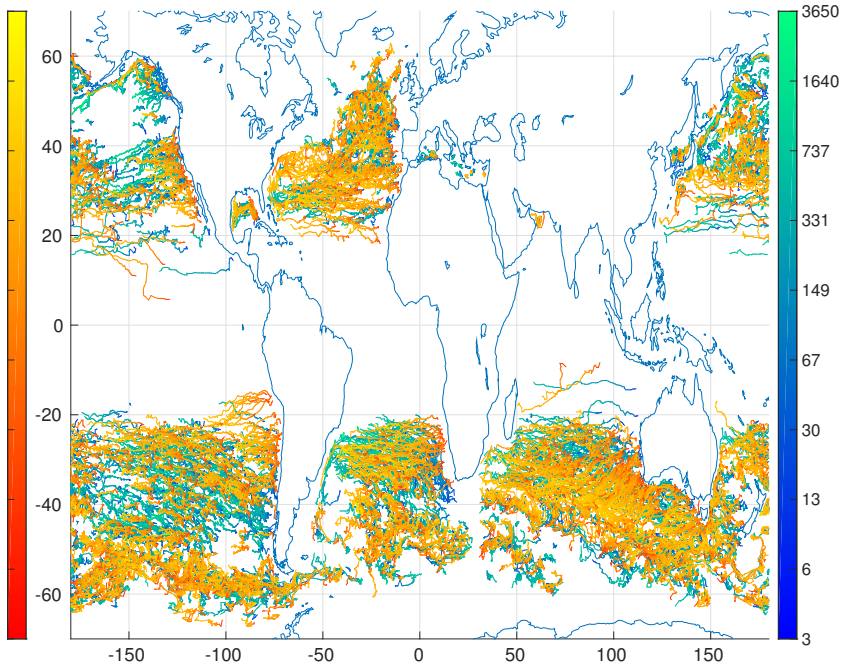


Figure 3.3: MI: anti-cyclones  
ind red. Tracks younger than 1a  
omitted for clarity.

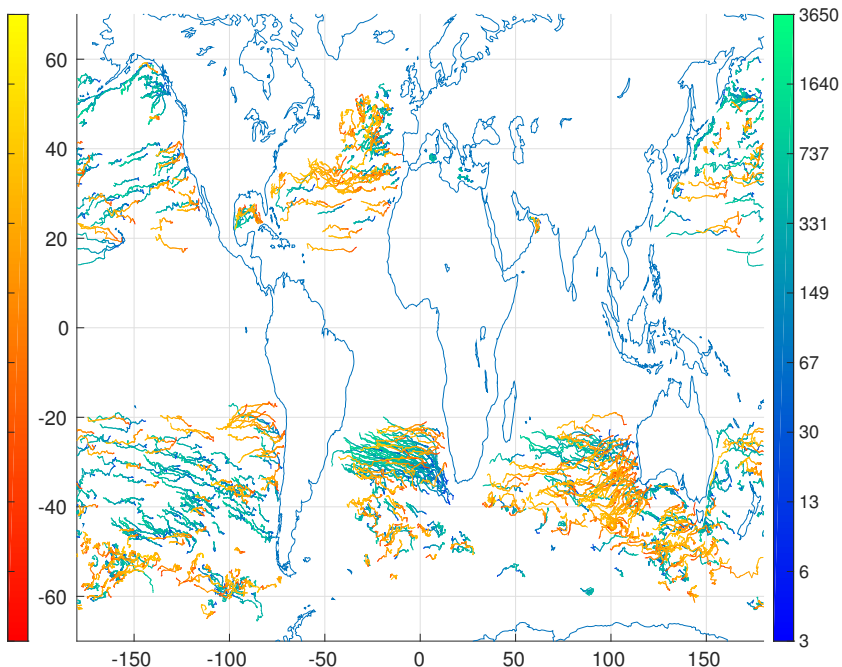


Figure 3.4: MII: anti-cyclones  
ind red. Tracks younger than 1a  
omitted for clarity.

The highest count of unique eddies is along the Antarctic Circumpolar Current <sup>1</sup> with counts of more than 60 individual eddy-visits per  $1^\circ \times 1^\circ$ -cell. Further eddy-rich regions are the western North-Atlantic throughout the Gulf-Stream and North-Atlantic Current, *Mozambique eddies* (?) at  $20^\circ$  South along the Mozambique coast, along the Agulhas Current and south of the Cup of Good Hope at  $\sim 40^\circ$ , along the coasts of Brazil, Chile and all along the Eastern, Southern and Western coasts of Australia (see Figure 3.7).

EDDIES APPEAR AND DISAPPEAR throughout the world ocean. For long-lived solid eddies there is a tendency to emerge along western coasts (see ??).

THE SCALE  $\sigma$  of tracked eddies is similar to that in ?, yet generally smaller in high latitudes and slightly larger in low latitudes (see ??). It is larger than the first-mode baroclinic Rossby Radius by factor of at least 2 and its meridional profile appears to be separable into two different regimes; one apparently linear profile in low latitudes and a steeper one equatorwards of  $\sim |15^\circ|$ . Regionally, locations of high meso-scale activity appear to correlate with smaller eddy-scales (see Figure 3.9).

THE EASTWARD ZONAL DRIFT SPEEDS are slightly slower than the first-mode baroclinic Rossby-Wave phase-speed and agree well with the results from ?. Propagations is generally west-wards except for regions of sufficiently strong eastward advection as in the ACC and North Atlantic Current (see Figure 3.10 and ??).

<sup>1</sup> abbreviated ACC from here on.

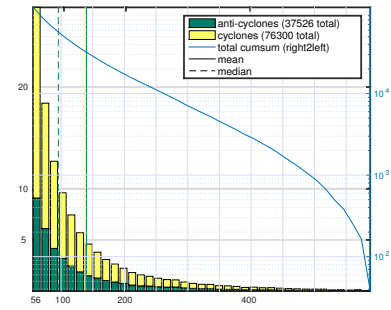


Figure 3.5: aviso-MI : Final age distribution. x-axis: [days], Left y-axis: [1000]

places of birth and death. size indicates final age.

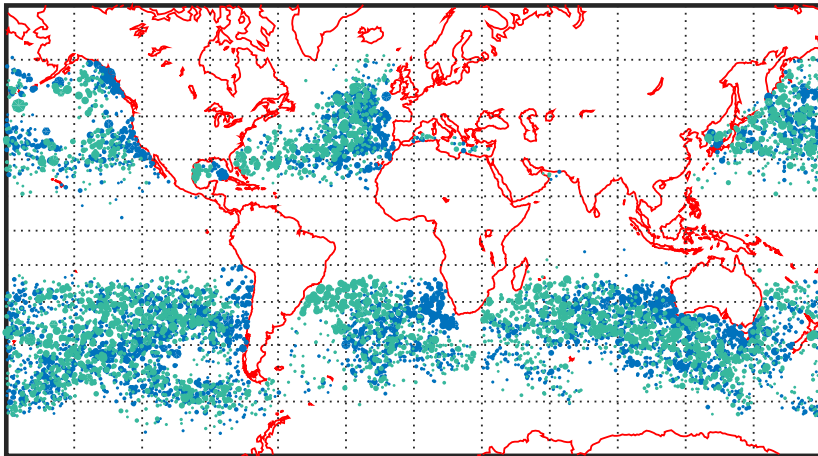


Figure 3.6: aviso-MI : Births are in blue and deaths in green. Size of dots scales to age squared. Only showing tracks older than one year.

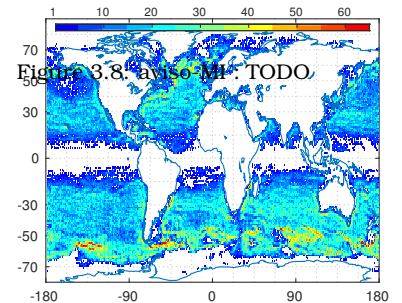
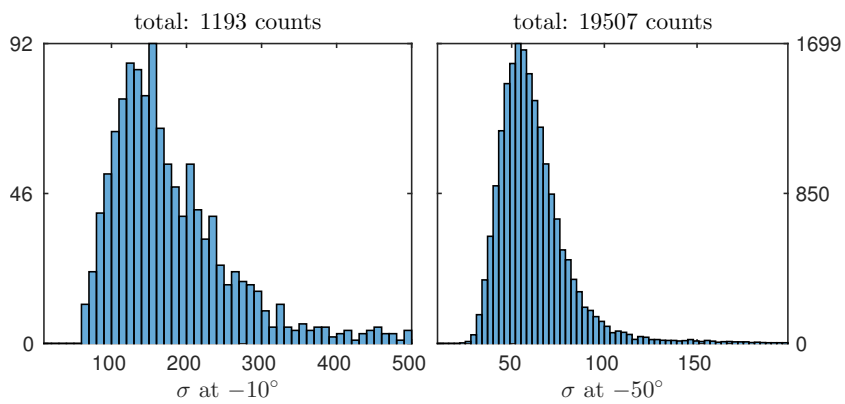


Figure 3.8: aviso-MI : TODO

Figure 3.7: aviso-MI : Total count of individual eddies per 1 degree square.

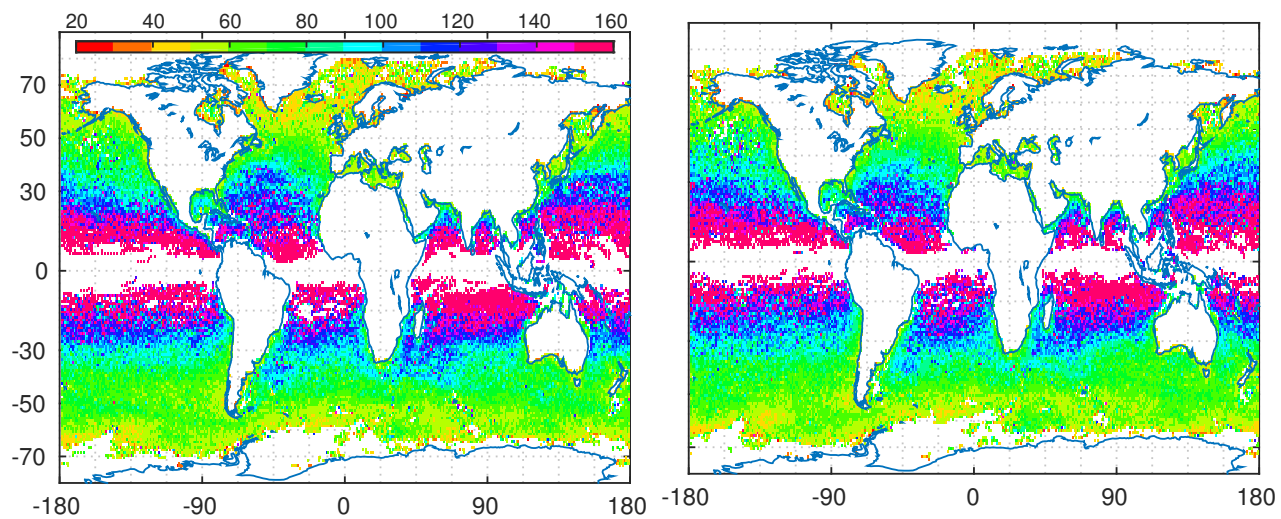


Figure 3.9: aviso-MI : TODO

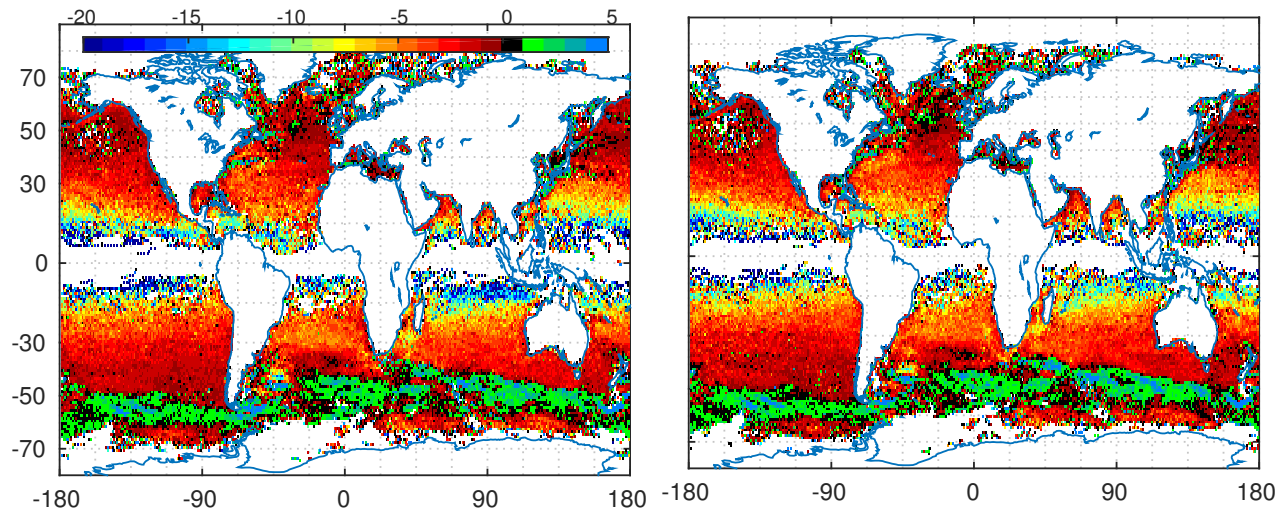


Figure 3.10: aviso-MI : TODO

### 3.2 MII - 7 day time-step - AVISO

THE IQ -BASED METHOD results in approximately the same total amount of tracks as the MI-method used in section 3.1 (see Figures 3.5 and 3.11). The difference is that tracks here are generally much shorter, meaning that less eddies are detected at any given point in time.

THE SCALE  $\sigma$  is now smaller than that from ? for all latitudes in zonal- mean as well as median.

WESTWARD DRIFT SPEEDS are almost identical to those in Section 3.1.

places of birth and death. size indicates final age.

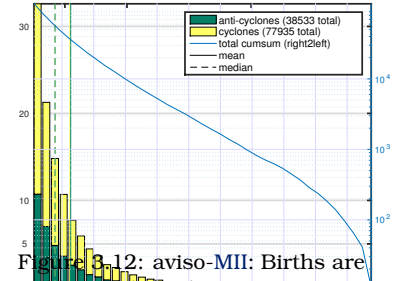
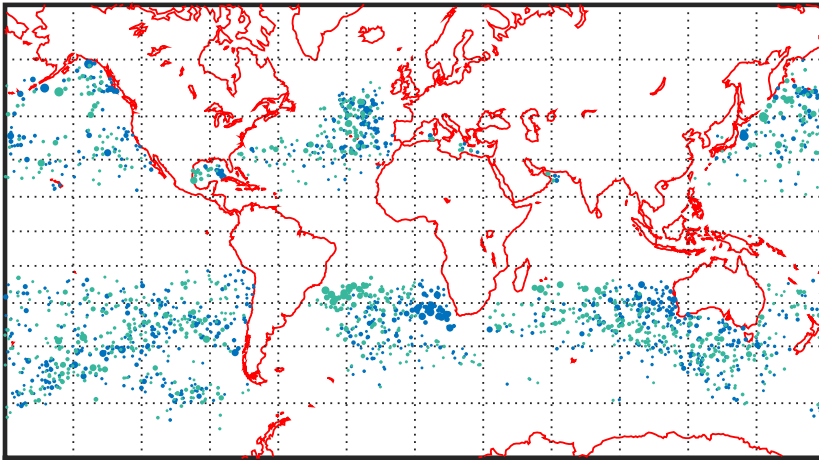


Figure 3.12: aviso-MII: Births are in blue and deaths in green. Size figure scales to average MII final age. Only showing tracks older than [days] per year. y-axis: [1000]

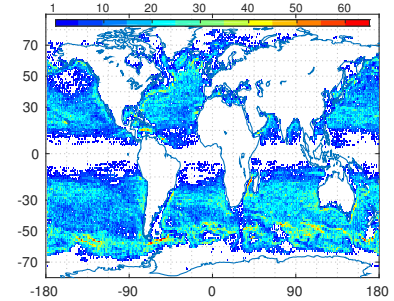


Figure 3.13: aviso-MII: Total count of individual eddies per 1 degree square.

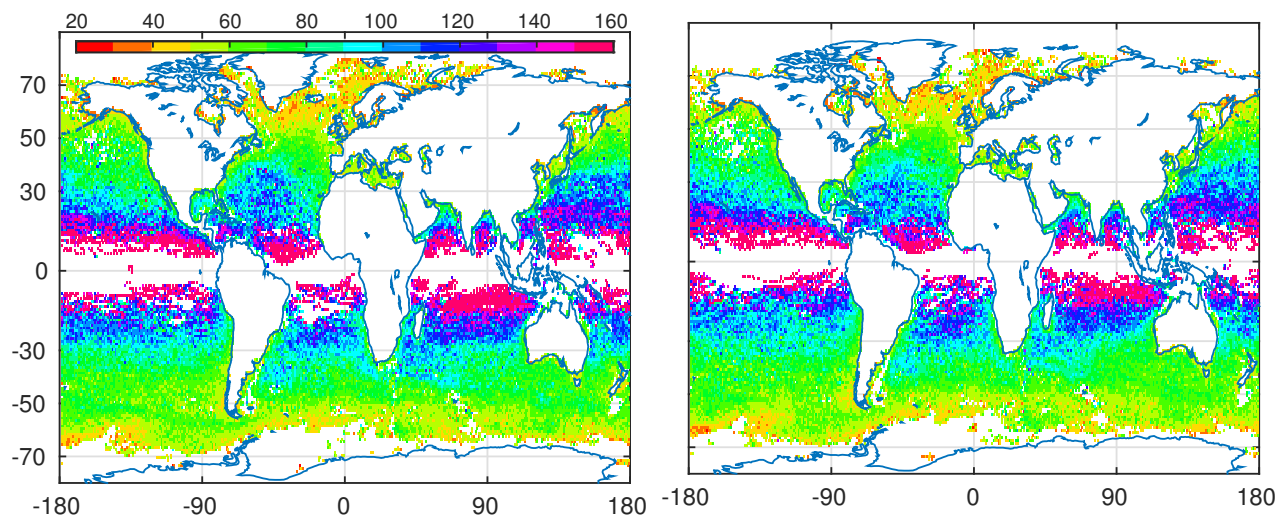


Figure 3.14: aviso-MII: TODO

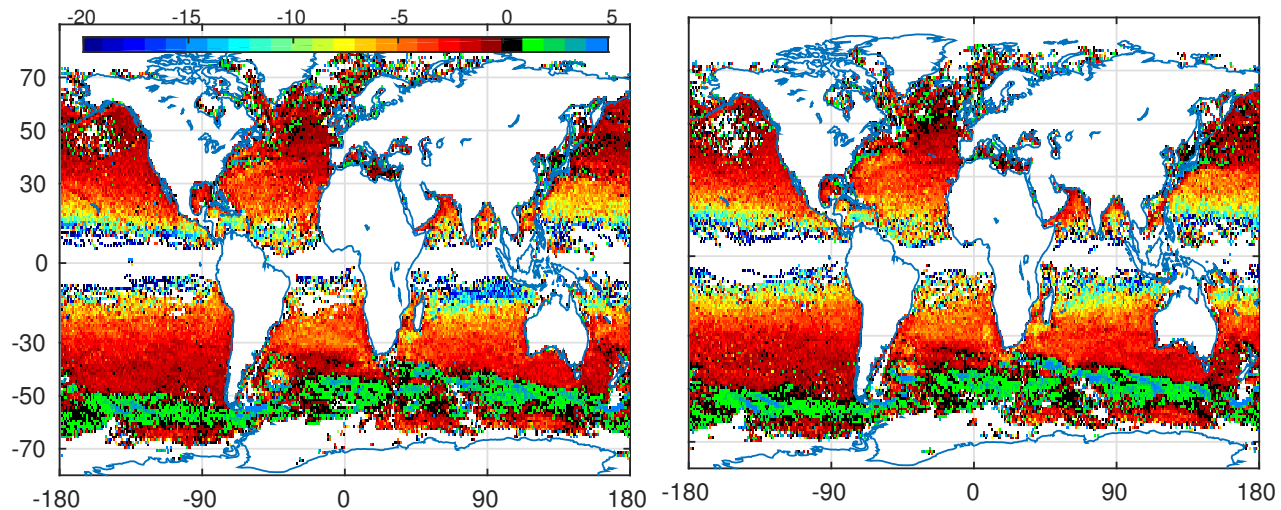


Figure 3.15: aviso-MII: TODO

### 3.3 MII - 7 day time-step - POP

THE MODEL DATA delivers slightly more total tracks with a similar 2-fold dominance of cyclones over anti-cyclones (compare Figures 3.11 and 3.16). Similar to aviso-MII very long tracks are fewer than via aviso-MI<sup>2</sup>. The regional pattern looks somewhat similar to the satellite patterns in terms of which regions feature the strongest eddy activity, with the exception of an unrealistic abundance of eddies right along the Antarctic coast where no eddies were detected for the satellite data likely due to sea ice and/or the inherent lack of polar data due to the satellites' orbit-inclinations. The more important difference between model- and satellite regional distributions is that the model results indicate significantly less eddy activity away from regions of strong SSH gradients, in the open ocean away from coasts and strong currents. The algorithm also detects hardly any eddy tracks in tropical regions (see ??).

THE SCALE  $\sigma$  is generally smaller for the model-data based analysis than for any satellite-based analyses, especially so in high latitudes.

WESTWARD DRIFT SPEEDS look regionally similar to those from satellite data (figs. 3.15 and 3.19). In the zonal mean their magnitude is below those from satellite (see Figure 3.22).

<sup>2</sup> aviso-MI features 3000 tracks that are older than 400 days, while both MII methods have only  $\sim 1000$  of such.

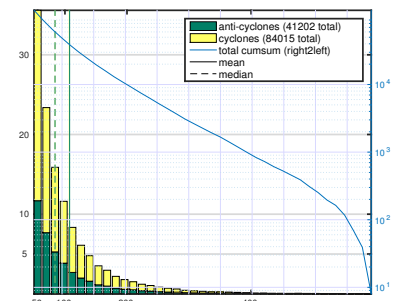


Figure 3.16: pop7-MII: Final age distribution. x-axis: [days], Left y-axis: [1000]

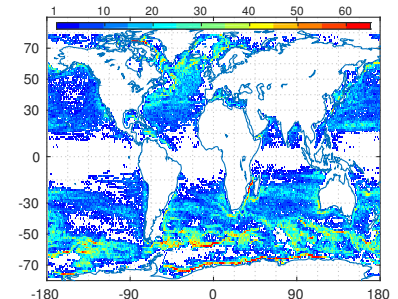


Figure 3.17: pop7-MII: Total count of individual eddies per 1 degree square.

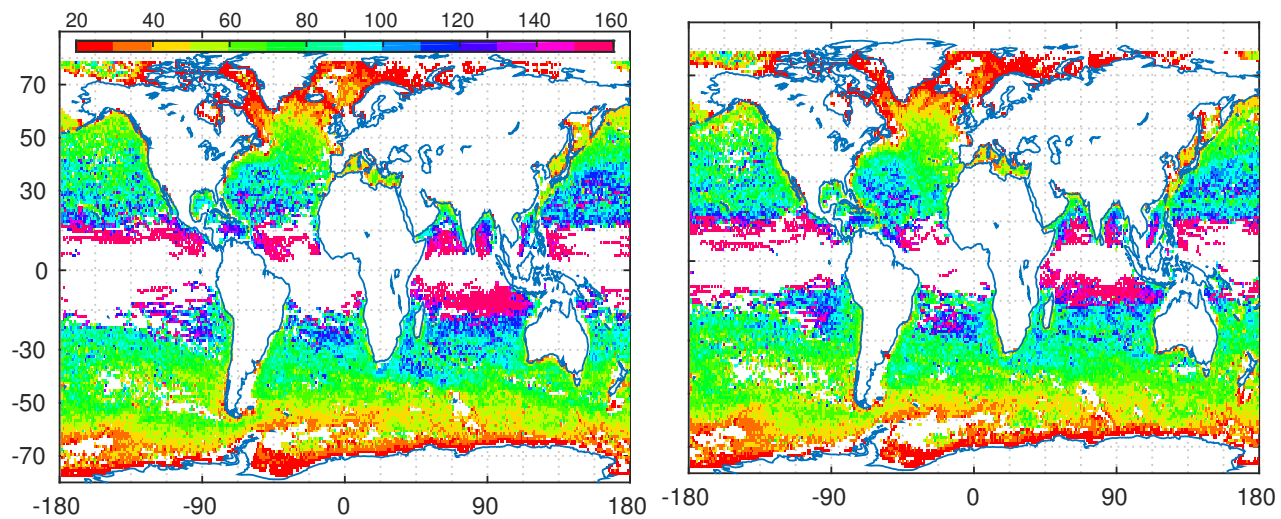


Figure 3.18: pop7-MII: TODO

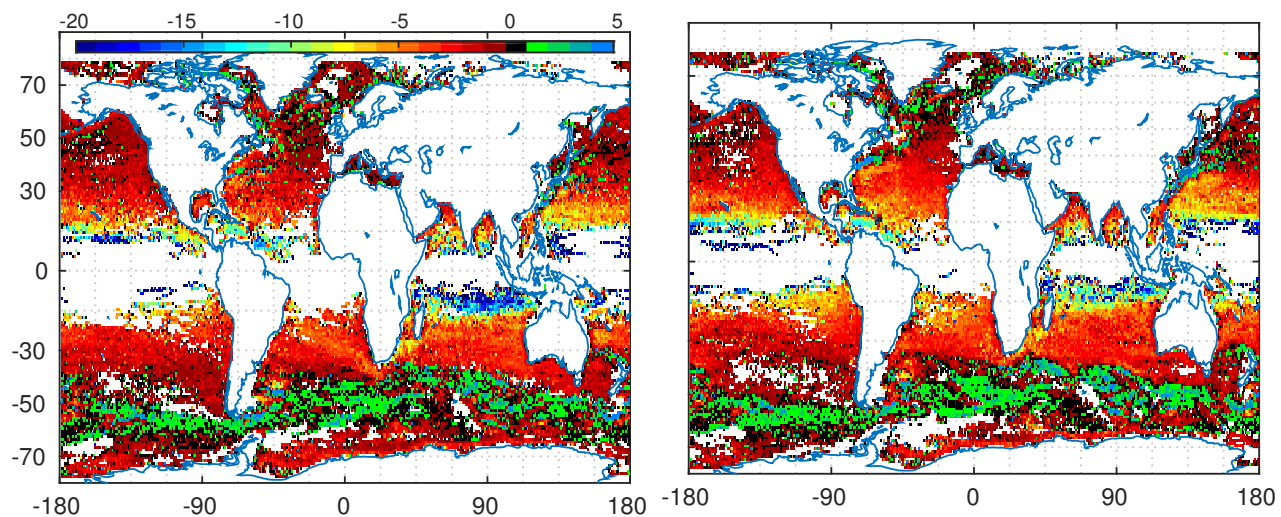


Figure 3.19: pop7-MII: TODO

### 3.4 MII - 7 day time-step - POP remapped to AVISO geometry

THE MODEL DATA

THE SCALE  $\sigma$

WESTWARD DRIFT SPEEDS

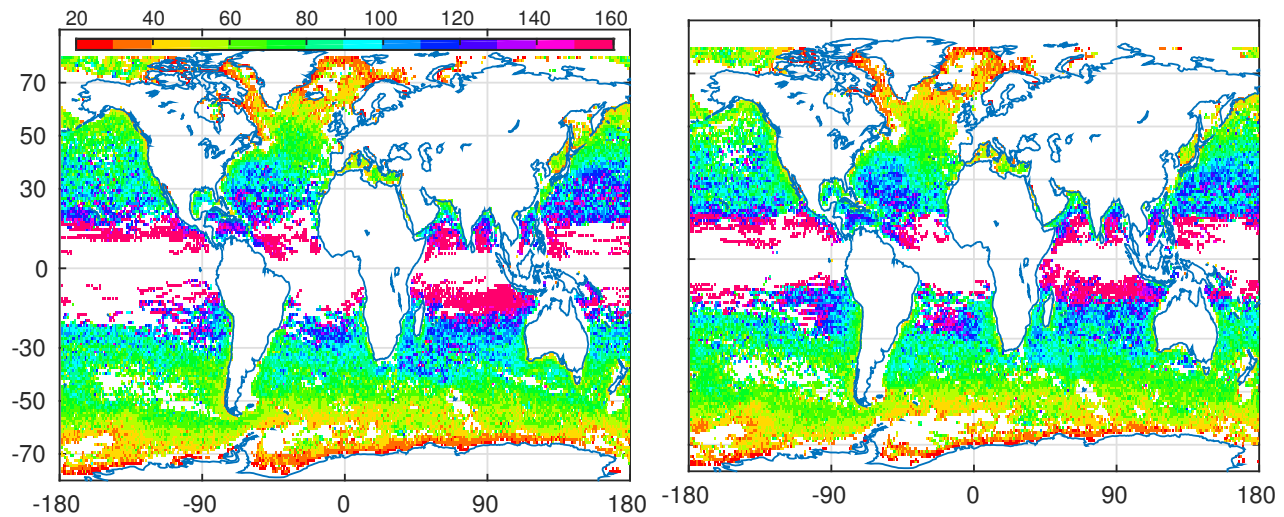


Figure 3.20: pop2aviso-MII: TODO

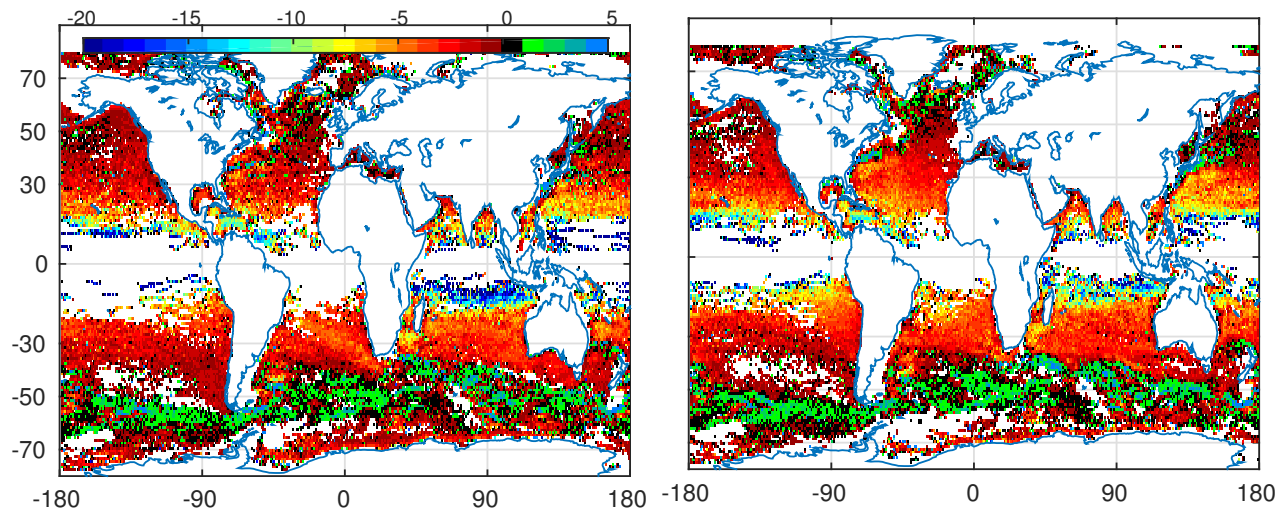


Figure 3.21: pop2aviso-MII: TODO

### 3.5 MII - 1 day time-step - POP

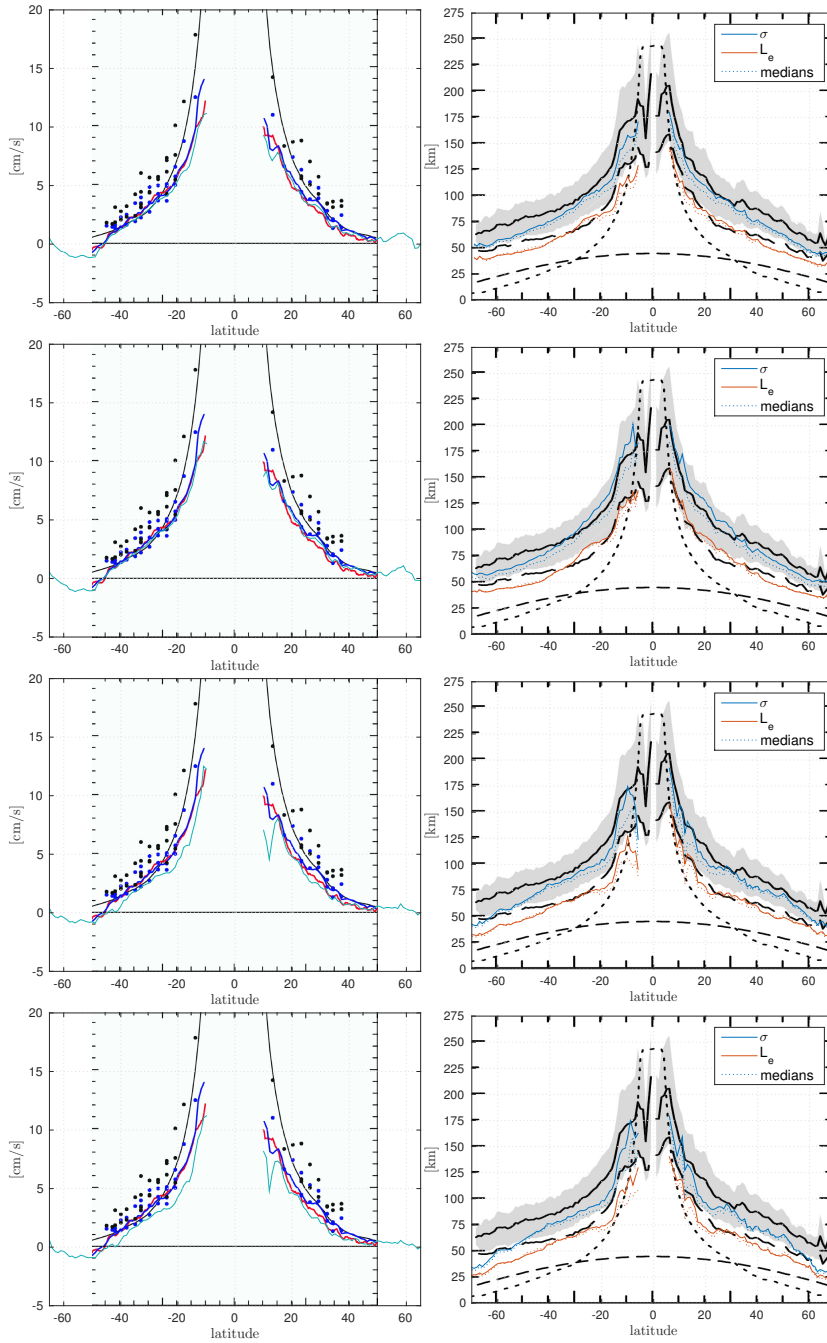


Figure 3.22: Left: Zonal-mean drift speed (cyan) fit to Fig 22 of [\(Chelton et al., 2011\)](#) (Background). Right:  $\sigma$  and  $L_e$  fit to Fig. 12 of their paper. Dotted lines are medians instead of means. 1st row: **aviso-MII**, 2nd row: **aviso-MI**, 3rd row: **pop2avi-MII**, 4th row: **POP-7day-MII**. Note that for the very high latitudes ( $> |60^\circ|$ ) the contrast between model and satellite data is further intensified by the lack of satellite data (see figs. 3.14 and 3.18) in those regions (sea-ice / orbit inclinations). For a depiction without this effect see fig. 4.2.

# 4

## Discussion

### 4.1 Lengths of Tracks

THE MOST APPARENT DIFFERENCE between the [two detection-methods](#) is the abundance of long-lived eddies resulting from the [MI](#)-method. The major difference between the two methods is the way in which the *shape* of found contour rings in SSH is decided to be sufficiently *eddy-like* or not (see filter 8).

THE [MI](#)-method is the more lenient one, as all it checks for, is whether the contour is of sufficiently compact form. The only shapes that are dismissed are long, thin elongated structures. This means that *e.g.* an eddy-track can more easily <sup>1</sup> survive situations in which two eddies merge into one or those in which one is split into two or situations in which mean current gradients distort the vortex.

There could also be the situation in which an old, weak eddy fades, yet another one emerges in sufficient proximity. These two events would not even have to coincide at the exact same time, as long as some short-lived coherent structure, of which there is an abundance <sup>2</sup> at any given time-step throughout the world ocean, acted as a *bridge* to fill the gap.

THE [MII](#)-method is conceptually different in that it is based on the assumption that a distinct coherent vortex need *per definition* to be more or less circular. It will therefore be more likely to regard *e.g.* the situation in which one eddy merges with another one as one of 3 eddies in total; **two** that have

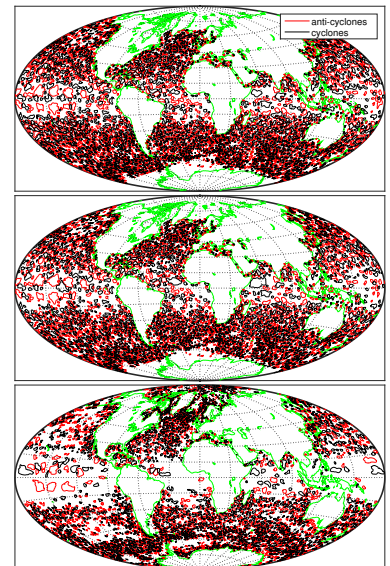


Figure 4.1: All contours that passed the filtering procedure for one exemplary time-step. Top: [aviso-MI](#) . Mid: [aviso-MII](#) . Bottom: [POP-7day-MII](#) .

<sup>1</sup> as long as the similarity-criterion is not violated.

<sup>2</sup> see ??

just died to create **one** new one. The focus here is more on the propagation of distinct circular geostrophic vortices whereas the focus in the **MI**-method is more general on coherent local depressions respective elevations in SSH. Unfortunately the time-frame of this work did not allow to test to which degree tracers<sup>3</sup> found within tracked eddies remained within the eddy over time. This could further clarify the assumption that the **MI**-method may be better at tracking water-mass advecting entities, with less jumps between bodies of water within one track.

## 4.2 Scales

INTERESTINGLY , even in the aviso-MI results, the horizontal eddy scale  $\sigma$  differs from that presented by [Chelton et al. \(2011\)](#). For latitudes  $\gtrsim |25^\circ|$  the zonal mean here is smaller than theirs while for low latitudes it is higher (see fig. 3.22). The reason for this discrepancy is suspected to stem from the special method by which  $\sigma$  is determined by our **TODO:our? my? this?** algorithm. As outlined in filter 12, here  $\sigma$  is half the mean of zonal and meridional distances between the first two local extrema of the first derivative of interpolated 4th-order fourier fits to the SSH data around the eddy's **CoV** . The motivation to use fits instead of the SSH directly was on the one hand to avoid noise complicating correct determinations of the 2nd differential zero-crossings and on the other hand to tackle the problem of coarse resolution, especially so for high latitudes where  $\sigma$  seems to become as small as only twice the distance between data points. At this resolution the *Gaussian RMS width* of an eddy would amount to only 5 data points. Since  $\sigma$  is generally smaller in the higher-resolution POP-data analyses, we hypothesize that the scales by [Chelton et al.](#) are biased high for high latitudes. Question remains to what degree this bias is inherent to the AVISO product *i.e.* as a smearing effect from the interpolation of multiple coarse satellite data. Or whether it is attributable entirely to the particular method by which the diameter/area of the zero-vorticity contour is estimated.

<sup>3</sup> in the model data.

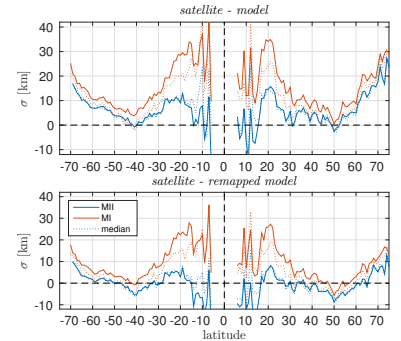


Figure 4.2: Differences in zonal mean  $\sigma$  between AVISO/POP and AVISO/downsampled POP. Means/Medians are built zonally over only those  $1^\circ \times 1^\circ$ -bins that feature data in both sets *i.e.* the intersection of  $\text{lat} + \text{lon}$  of both sets.

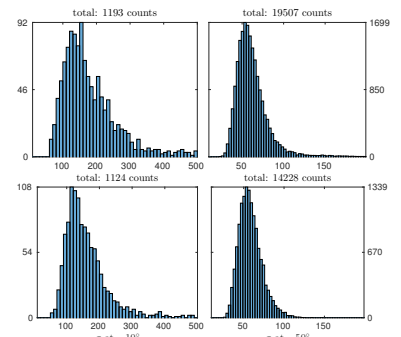


Figure 4.3: Eddy count at one point in time for one fully zonal  $1^\circ$ -bin. Top: aviso-MI . Bottom: aviso-MII . The tropical spectrum is broad yet with strong positive skewness *i.e.* oriented towards smaller scales. In high latitudes the standard deviation is smaller. The **MI** method yields more large eddies.

WITH REGARD to the lower latitudes two important aspects need to be considered:

1. The analyses yield generally low eddy activity in the tropics.  
Hence the results are less robust in this region *a priori*.
2. The standard deviation in  $\sigma$  is particularly broad in the tropics (see fig. 4.3). As a matter of fact it appears as though there might be two different types of eddies. One type analogous to all high-latitude eddies and a new one of much larger scale. Because these larger eddies have generally low IQ-values they are filtered from the MII analyses, resulting in smaller tropical  $\sigma$ . Their more chaotic shape might, due to the different methods to determine  $\sigma$ , also have to do with why mean tropical  $\sigma$  is larger here than in Chelton *et al.* (2011).

THE POP-7day-MII analysis yields somewhat similar  $\sigma$  for low latitudes <sup>4</sup>, yet significantly smaller values for high latitudes. The question therefore is whether this discrepancy is a result of the lower resolution of the satellite data *i.e.*

that eddies are too small to be resolved by the AVISO product in high latitudes or whether it is attributable to the model data as in a systematic bias due to incomplete/poorly parameterised model physics. This question was the primary motivation for the pop2avi-MII -analysis. The idea here was to down-size the POP data to the geometry of the AVISO grid in order to test whether this would raise  $\sigma$  to that from the satellite results.

Figure 4.2 shows that the down-sampling did indeed decrease the discrepancy in  $\sigma$  to respective AVISO analysis, as long as those regions that are unique to either data set are excluded. Between  $\pm 25^\circ$  and  $\pm 65^\circ$  the difference is no larger than  $\pm 5\text{km}$ . This came as a surprise because since  $\sigma$  stems from fourier fits of SSH, we expected the original frequencies to be, at least to some extent, conserved in the down-sampled data.

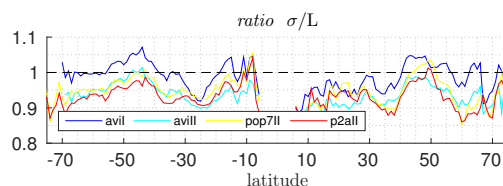


Figure 4.4: Ratios if  $\sigma$  to  $L$  (see filter 10)

<sup>4</sup> Note that due to the lack of tropical eddies the estimates of  $\sigma$  are rather uncertain for the POP analyses.

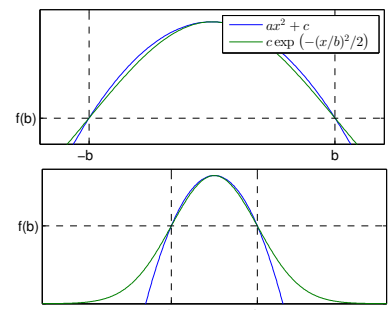


Figure 4.5: The upper part of a Gaussian profile can appear similar to a quadratic one.

THE MI detection method a priori assumes that an eddy is more or less detected at its asymptotic *floor* i.e. in the case of an anti-cyclone at the *foot of the mountain*. The idea of the IQ -based method on the other hand is to assume that the situation of a single well-defined eddy sitting on an otherwise smooth, flat sea surface, which would be necessary for the contour algorithm to find a closed contour describing the outermost perimeter of said single vortex, is unrealistic. Instead the approach is to look for distinct, sufficiently circular *caps* of SSH- hills respepective valleys that consistently *wade* through all other weaker geostrophic noise surrounding it. **TODO: why gaussian or quad?**

### 4.3 Drift Speeds

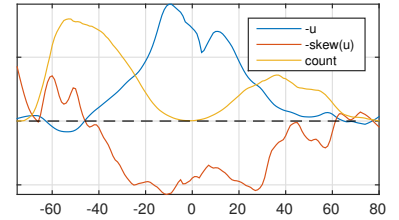


Figure 4.6: TODO

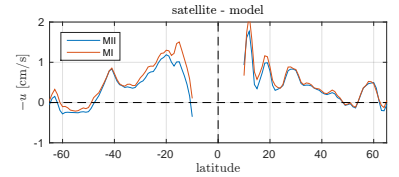


Figure 4.7: TODO:caption

# A

## Turbulence Aspects

The horizontal scales of planetary geostrophic turbulence are usually so much larger than the vertical, that due to the gyroscopic rigidity of fluid motion in a rotating frame of reference, the turbulence is practically invariant in the vertical. Two-dimensional motion has the odd, counter-intuitive quality of cascading towards **larger** instead of **smaller** scales, as would be expected from 3-dimensional flow. This appendix is an attempt to explain this peculiar phenomenon heuristically.

$$\frac{Du}{Dt} + \Omega \times u = -\frac{1}{\rho} \nabla p + v \nabla^2 u + g \quad (\text{A.1a})$$

$$\frac{Dm}{Dt} = 0 \quad (\text{A.1b})$$

$$\frac{D\omega_a}{Dt} = (\omega_a \cdot \nabla) u + B + v \nabla^2 \omega \quad (\text{A.1c})$$

$$\frac{DE_k}{Dt} = -u_h \cdot \frac{1}{\rho} \nabla_h p + v \left( \frac{1}{2} \nabla^2 u^2 - \|\nabla u\|^2 \right) \quad (\text{A.1d})$$

$$\frac{DE_m}{Dt} = v \left( \frac{1}{2} \nabla^2 u^2 - \|\nabla u\|^2 \right) \quad (\text{A.1e})$$

$$\frac{D\varepsilon}{Dt} = \omega \cdot (\omega_a \cdot \nabla) u + \omega \cdot v \nabla^2 \omega \quad (\text{A.1f})$$

Consider the equations of motion on a rotating spherical planet with all body forces combined in  $g$ , which shall always be perpendicular to the surface of a Newtonian fluid at rest. Applying the curl to equation (A.1a) also yields a vorticity equation<sup>1</sup>. Scalar multiplication with  $u$  reveals a prognostic, kinetic-energy-per-unit-mass budget<sup>2</sup>. Analogously, scalar multiplication of equation (A.2c) with  $\omega_a$  yields an equation for the macroscopic enstrophy density per unit mass<sup>3</sup>. Finally, adding a term for potential energy to equation (A.1d) yields an equation for mechanical energy<sup>4</sup>.

<sup>1</sup> see Derivation ?? 1

<sup>2</sup> see Derivation ?? 2

<sup>3</sup> see Derivation ?? 4

<sup>4</sup> see Derivation ?? 3

### Turbulence A.1: Non-rotating Tank

Consider first a 3 dimensional non-rotating volume of fluid of constant density with horizontal and vertical dimensions of equal scale. Equations (A.1) then reduce to (ignoring  $E_k$ ):

$$\frac{Du}{Dt} = -\frac{1}{\rho} \nabla p + v \nabla^2 u + g \quad (\text{A.2a})$$

$$\nabla \cdot u = 0 \quad (\text{A.2b})$$

$$\frac{D\omega}{Dt} = (\omega \cdot \nabla) u + v \nabla^2 \omega \quad (\text{A.2c})$$

$$\frac{DE_m}{Dt} = v \left( \frac{1}{2} \nabla^2 u^2 - \|\nabla u\|^2 \right) \quad (\text{A.2e})$$

$$\frac{D\varepsilon}{Dt} = \omega \cdot (\omega \cdot \nabla) u + \omega \cdot v \nabla^2 \omega \quad (\text{A.2f})$$

If we further assume the viscosity  $v$  of the fluid to be infinitely small equation (A.2e) and equation (A.2f) reduce to

$$\frac{DE_m}{Dt} = 0 \quad (\text{A.3e})$$

$$\frac{D\varepsilon}{Dt} = \omega \cdot (\omega \cdot \nabla) u \quad (\text{A.3f})$$

In the absence of friction the mechanical Energy of the parcel of fluid is conserved.

In contrast, neither enstrophy nor vorticity itself are conserved. Velocity gradients will tilt and stretch the parcel resulting in changes in relative vorticity so as to conserve the parcel's total angular momentum. There is no preference for dimension. The motion is simply turbulent akin to air blowing through a room.

### Turbulence A.2: Rotating Tank

Next consider the tank from ?? A.1 to be rotating at some high constant frequency  $\Omega/2 \hat{z}$ , so that all terms void of  $\Omega$  are small versus those containing  $\Omega$  while all derivatives of  $\Omega$  vanish for its constancy. Again, imagine some magical mix of body forces, so that  $g \cdot \hat{z} = -g$ .

$$\frac{Du_h}{Dt} = -\Omega \times u_h + g \nabla \eta \quad (\text{A.4a})$$

$$\frac{D\omega}{Dt} = \Omega \frac{\partial u}{\partial z} \quad (\text{A.4c})$$

$$\frac{DE_m}{Dt} = v \left( \frac{1}{2} \nabla^2 u^2 - \|\nabla u\|^2 \right) \quad (\text{A.4e})$$

$$\frac{D\varepsilon}{Dt} = \omega \cdot \Omega \frac{\partial u}{\partial z} \quad (\text{A.4f})$$

Equation (A.4a) reveals that in this case all motion must be perpendicular to  $\Omega$  and to pressure gradients. Hence  $w \approx 0$  and  $u_h$  in hydrostatic- and geostrophic balance. Equation (A.4c) shows how a stretched or squeezed water column by e.g. a change in water depth results in a dramatic change in relative vorticity. Equation (A.4e) and equation (A.4f) show that again energy is conserved for the  $Re \gg 1$  case (since our perspective is from the rotating frame of reference, the angular momentum

from the rotating tank is a priori irrelevant to  $E_m$ ), and that local enstrophy of a Lagrangian parcel is dramatically changed as soon as the vertical dimension is forced upon the motion.

### Turbulence A.3: Small Aspect Ratio

Consider again the tank, only this time completely flattened, so that its horizontal extent is, say, 3 orders of magnitude larger than its vertical scale. All vertical motion then becomes insignificant and at first approximation the equations reduce to:

$$\frac{\partial \mathbf{u}}{\partial t} + \mathbf{u} \cdot \nabla \mathbf{u} = g \nabla \eta + \nu \nabla^2 \mathbf{u} \quad (\text{A.5a})$$

$$\frac{\partial \omega}{\partial t} + \mathbf{u} \cdot \nabla \omega = \nu \nabla^2 \omega \quad (\text{A.5c})$$

$$\frac{DE_m}{Dt} = \nu \left( \frac{1}{2} \nabla^2 \mathbf{u}^2 - \omega^2 \right) \quad (\text{A.5e})$$

$$\frac{D\varepsilon}{Dt} = \nu \left( \frac{1}{2} \nabla^2 \omega^2 - \|\nabla \omega\|^2 \right) \quad (\text{A.5f})$$

The main point here is that now, for infinitely small viscosity, besides mechanical energy, now also enstrophy is materially conserved. Lacking a third dimension to stretch, squeeze or tilt into, a column of fluid has no mechanism by which to adapt to a change in depth or to a change in ambient vorticity. To investigate this situation further, a scale analysis of the equations of  $E_m$  and  $\varepsilon$  is helpful:

$$\frac{U^2}{T} + \frac{U^3}{L} = \frac{\nu U^2}{L^2} \quad (\text{A.6e})$$

$$\frac{U^2}{TL^2} + \frac{U^3}{L^3} = \frac{\nu U^2}{L^4} \quad (\text{A.6f})$$

Apparently  $\frac{DE_m}{Dt} \sim L^2 \frac{D\varepsilon}{Dt}$ . Thus, the smaller  $L$ , the more effective vorticity is advected and burned. Hence enstrophy dominates the turbulence cascade towards smaller scales. Before  $E_m$  gets any chance to cascade itself to ever smaller scales,  $\varepsilon$  is already effectively burning vorticity at large  $k$  and thereby reducing kinetic energy faster than the turbulence cascade can fill the gap.  $E_m$  being proportional to  $U^2$  cannot compete with  $\varepsilon$  at small scales since  $\varepsilon$  not only scales with  $U^2$  but also with the squared reciprocal of the scale *itself*.

As an analogy consider an ice hockey arena being opened instantaneously to 500 people on skates. At first the picture will be highly turbulent with lots of friction among skaters. Sooner or later though, people of like-minded preference for direction and speed are likely to form groups so as to avoid bumping into one another. At some point usually all the people form into one or few large eddies, with those wanting to go faster than others skating at larger radius than the more timid towards the center, whilst those on inadequate orbits usually get automatically advected accordingly.

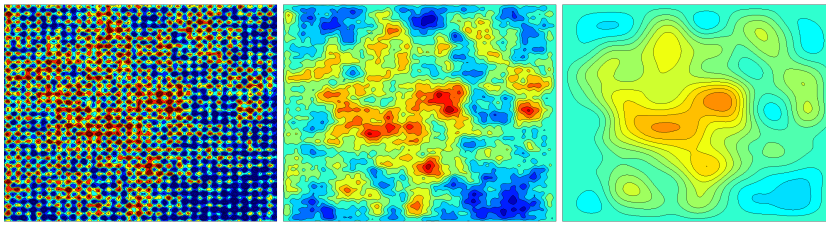


Figure A.1: 1) 2D turbulence with several sinusoidal and random signals as initial condition, 2) at a later time 3) at a much later time. Code from ?.

**Turbulence A.4:  $\beta$ -effect**

Consider at last the inviscid rotating flat-disk-type tank this time in the shape of a shell of a sphere with again  $\mathbf{g} \parallel \mathbf{z}$  everywhere perpendicular to the surface at rest. Further assume a strong  $\mathbf{g}$  so that the  $\boldsymbol{\Omega} \cdot \mathbf{y}$  component in the Coriolis term is dwarfed by hydrostaticity. Then with  $\mathbf{f} = fz = (\boldsymbol{\Omega} \cdot \mathbf{z}) \mathbf{z}$  now from a Eulerian perspective:

$$\frac{\partial \mathbf{u}}{\partial t} = -\mathbf{u} \cdot \nabla \mathbf{u} - \mathbf{f} \times \mathbf{u} + g \nabla \eta \quad (\text{A.7a})$$

$$\frac{\partial \omega}{\partial t} = -\mathbf{u}_h \cdot \nabla_h \omega - v \frac{\partial f}{\partial y} \quad (\text{A.7c})$$

A new term with opposite sign from the  $\omega$ -advection-term in  $y$ -direction arises in the vorticity budget, which is evidently most significant where  $f$  changes strongest meridionally, *i.e.* In proximity to the sphere's *equator*. Hence, if scales permit, relative vorticity can now also be altered by a change in latitude via conservation of angular momentum.

# B

## Derivations

### Derivation 1: Vorticity

With the identity

$$\begin{aligned}\mathbf{u} \cdot \nabla \mathbf{u} &= (\nabla \times \mathbf{u}) \times \mathbf{u} + \nabla |\mathbf{u}|^2 / 2 \\ &= \boldsymbol{\omega} \times \mathbf{u} + \nabla \mathbf{u}^2 / 2\end{aligned}\quad (\text{B.1})$$

equation (A.1a) becomes

$$\begin{aligned}\frac{\partial \mathbf{u}}{\partial t} + \nabla |\mathbf{u}|^2 / 2 + (2\boldsymbol{\Omega} + \boldsymbol{\omega}) \times \mathbf{u} &= -\frac{1}{\rho} \nabla p + \nu \nabla^2 \mathbf{u} + \mathbf{g} \\ \frac{\partial \mathbf{u}}{\partial t} + \nabla |\mathbf{u}|^2 / 2 + \boldsymbol{\omega}_a \times \mathbf{u} &= -\frac{1}{\rho} \nabla p + \nu \nabla^2 \mathbf{u} + \mathbf{g}\end{aligned}\quad (\text{B.2})$$

Applying the curl operation to equation (A.1a) and assuming equation (A.1b) for an incompressible fluid yields an equation for the vorticity

$$\begin{aligned}\frac{\partial \boldsymbol{\omega}}{\partial t} + \nabla \times \nabla |\mathbf{u}|^2 / 2 + \nabla \times (\boldsymbol{\omega}_a \times \mathbf{u}) &= \\ = -\frac{1}{\rho} \nabla \times \nabla p - \nabla \rho^{-1} \times \nabla p + \nu \nabla \times \nabla^2 \mathbf{u} + \nabla \times \mathbf{g} &\quad (\text{B.3})\end{aligned}$$

Annihilating all  $\nabla \times \text{grad}$  and  $\nabla \cdot \nabla \times$  and making use of the identity

$$\nabla \times (\mathbf{A} \times \mathbf{B}) = \mathbf{A} (\nabla \cdot \mathbf{B}) - \mathbf{B} (\nabla \cdot \mathbf{A}) + (\mathbf{B} \cdot \nabla) \mathbf{A} - (\mathbf{A} \cdot \nabla) \mathbf{B} \quad (\text{B.4})$$

equation (B.3) becomes

$$\begin{aligned}
 \frac{\partial \omega}{\partial t} + \nabla \times (\omega_a \times \mathbf{u}) &= -\frac{\nabla p \times \nabla p}{\rho^2} + \nu \nabla \times \nabla^2 \mathbf{u} \\
 \frac{\partial \omega}{\partial t} + (\mathbf{u} \cdot \nabla) \omega_a - \mathbf{u} (\nabla \cdot \omega_a) - (\omega_a \cdot \nabla) \mathbf{u} \\
 &\quad = \mathbf{B} - \nu \nabla \times (\nabla \times (\nabla \times \mathbf{u})) \\
 \frac{D\omega_a}{Dt} &= (\omega_a \cdot \nabla) \mathbf{u} + \mathbf{B} - \nu \nabla \times (\nabla \times \omega) \\
 &= (\omega_a \cdot \nabla) \mathbf{u} + \mathbf{B} + \nu \nabla^2 \omega
 \end{aligned} \tag{B.5}$$

Scaling considerations based on the small aspect ratio e.g. noting that  $\mathbf{B} \sim \nabla p \times \nabla p$  is at first approximation limited to the  $x, y$  plane and that  $U/H \gg W/L$  and assuming  $\omega_z \gg \omega_h$ , leads to:

$$\frac{\partial \omega}{\partial t} + \mathbf{u} \cdot \nabla \omega + \beta v \hat{z} = (\omega_z + f) \frac{\partial \mathbf{u}}{\partial z} + \mathbf{B} \tag{B.6}$$

horizontal:

$$\begin{aligned}
 \frac{1}{T} \frac{U}{H} + \left( \frac{U}{L} + \frac{W}{H} \right) \frac{U}{H} &\sim \frac{U}{H} \frac{U}{L} + f \frac{U}{H} + \mathbf{B} \\
 \Rightarrow \frac{U}{HT} + \frac{U^2}{LH} + \frac{UW}{H^2} &\sim \frac{U^2}{LH} + f \frac{U}{H} + \mathbf{B}
 \end{aligned} \tag{B.7}$$

vertical:

$$\begin{aligned}
 \frac{U}{LT} + \frac{U^2}{L^2} + \frac{WU}{HL} + \beta V &\sim \frac{UW}{LH} + f \frac{W}{H} \\
 \Rightarrow \frac{U}{LT} + \frac{U^2}{L^2} + \beta V &\sim \frac{WU}{HL} + f \frac{W}{H}
 \end{aligned} \tag{B.8}$$

Hence at first order:

$$\frac{D\omega_h}{Dt} = (f + \omega_z) \frac{\partial \mathbf{u}_h}{\partial z} + \mathbf{B} \tag{B.9}$$

$$\frac{D\omega_z}{Dt} + \beta v = (f + \omega_z) \frac{\partial \omega}{\partial z} \tag{B.10}$$

$\omega_h$  is due to small ageostrophic parallelization of  $\nabla p$  and  $\nabla \rho$  via  $\mathbf{B}$  the tilting terms vanish, since then  $\omega_h$  normal to the plane spanned by  $\nabla \mathbf{u}_h$  and  $\nabla w$

## Derivation 2: Kinetic Energy

Multiply equation (A.1a) by  $\mathbf{u}$ :

$$\begin{aligned}
 \mathbf{u} \cdot \left( \frac{\partial \mathbf{u}}{\partial t} + \mathbf{u} \cdot \nabla \mathbf{u} + 2\Omega \times \mathbf{u} \right) &= -\mathbf{u} \cdot \frac{1}{\rho} \nabla p + \mathbf{u} \cdot \nu \nabla^2 \mathbf{u} + \mathbf{u} \cdot \mathbf{g} \\
 \frac{1}{2} \frac{\partial \mathbf{u}^2}{\partial t} + \frac{1}{2} \mathbf{u} \cdot \nabla \mathbf{u}^2 + \mathbf{u} \cdot 2\Omega \times \mathbf{u} &= -\mathbf{u} \cdot \frac{1}{\rho} \nabla p + \mathbf{u} \cdot \nu \nabla^2 \mathbf{u} - w g \\
 \frac{1}{2} \frac{\partial \mathbf{u}^2}{\partial t} + \frac{1}{2} \mathbf{u} \cdot \nabla \mathbf{u}^2 &= -\mathbf{u}_h \cdot \frac{1}{\rho} \nabla_h p + w g + \mathbf{u} \cdot \nu \nabla^2 \mathbf{u} - w g \\
 \frac{1}{2} \frac{\partial \mathbf{u}^2}{\partial t} + \frac{1}{2} \mathbf{u} \cdot \nabla \mathbf{u}^2 &= -\mathbf{u}_h \cdot \frac{1}{\rho} \nabla_h p + \mathbf{u} \cdot \nu \nabla^2 \mathbf{u} \\
 \frac{\partial E_k}{\partial t} + \mathbf{u} \cdot \nabla E_k &= -g \mathbf{u}_h \cdot \nabla \eta(x, y) + \nu \left( \frac{1}{2} \nabla^2 \mathbf{u}^2 - \|\nabla \mathbf{u}\|^2 \right)
 \end{aligned} \tag{B.11}$$

### Derivation 3: Mechanical Energy

Add term for potential energy to equation (A.1d) (assuming  $\nabla \rho = 0$ )

$$\begin{aligned}
 \frac{DE_m}{Dt} &= -g \mathbf{u} \cdot \nabla \eta(x, y) + \nu \left( \frac{1}{2} \nabla^2 \mathbf{u}^2 - \|\nabla \mathbf{u}\|^2 \right) + \mathbf{u} \cdot \mathbf{g} \\
 \frac{DE_m}{Dt} &= -g \mathbf{u} \cdot \nabla \eta(x, y) + \nu \left( \frac{1}{2} \nabla^2 \mathbf{u}^2 - \|\nabla \mathbf{u}\|^2 \right) - w g \\
 &= -g \left( \frac{\partial \eta}{\partial t} + \mathbf{u} \cdot \nabla \eta \right) + \nu \left( \frac{1}{2} \nabla^2 \mathbf{u}^2 - \|\nabla \mathbf{u}\|^2 \right) \\
 &= -g \frac{D\eta}{Dt} + \nu \left( \frac{1}{2} \nabla^2 \mathbf{u}^2 - \|\nabla \mathbf{u}\|^2 \right) \\
 &= \nu \left( \frac{1}{2} \nabla^2 \mathbf{u}^2 - \|\nabla \mathbf{u}\|^2 \right)
 \end{aligned} \tag{B.12}$$

### Derivation 4: Enstrophy

In 2 dimensions the definition of enstrophy can also be rewritten as:

$$\begin{aligned}
 \mathcal{E} &= \int_A \varepsilon \, dA = \int_A \|\nabla \mathbf{u}\|^2 \, dA \\
 &= \int_A \left( \frac{\partial v}{\partial x} \right)^2 + \left( \frac{\partial u}{\partial y} \right)^2 + \left( \frac{\partial v}{\partial y} \right)^2 + \left( \frac{\partial u}{\partial x} \right)^2 \, dA \\
 &= \int_A \left( \frac{\partial v}{\partial x} \right)^2 + \left( \frac{\partial u}{\partial y} \right)^2 + \left( \frac{\partial v}{\partial y} \right)^2 + \left( \frac{\partial u}{\partial x} \right)^2 - (\nabla \cdot \mathbf{u})^2 \, dA \\
 &= \int_A \left( \frac{\partial v}{\partial x} \right)^2 + \left( \frac{\partial u}{\partial y} \right)^2 - 2 \frac{\partial u}{\partial x} \frac{\partial v}{\partial y} \, dA \\
 &= \int_A \omega^2 + 2 \frac{\partial u}{\partial y} \frac{\partial v}{\partial x} - 2 \frac{\partial u}{\partial x} \frac{\partial v}{\partial y} \, dA \\
 &= \int_A \omega^2 + 2 \frac{\partial u}{\partial y} \frac{\partial v}{\partial x} + 2 \left( \frac{\partial v}{\partial y} \right)^2 \, dA
 \end{aligned} \tag{B.13}$$

with  $\nabla \cdot \mathbf{u} = 0$  and appropriate boundary conditions, the last two terms cancel in the integral leaving

$$\mathcal{E} = \int_A \omega^2 \, dA \tag{B.14}$$

### Derivation 5: Vorticity Scales

Assuming approximate geostrophy and  $Bu = \mathcal{O}(10^1)$ :

$$\rho f U \sim \nabla p \tag{B.15}$$

in a layered model:

$$\begin{aligned}
 fU &\sim g' \nabla \eta \\
 U &\sim \frac{hN^2}{f} \nabla \eta \\
 U &\sim \frac{h^2 N^2}{fL}
 \end{aligned} \tag{B.16}$$

and hence

$$\begin{aligned}
 \omega &\sim U/L \sim \frac{h^2 N^2}{fL^2} \\
 &= \frac{h^2 N^2}{fL_R^2} \frac{L_R}{L} \\
 &= f \frac{L_R}{L}
 \end{aligned} \tag{B.17}$$

### Derivation 6: vortex limitations

$$\mathbf{u} \cdot \nabla \mathbf{u} + f \mathbf{u} = -g \nabla \eta \quad (\text{B.18})$$

$$\begin{aligned} \frac{U^2}{L} + fU + \frac{gh}{L} &= 0 \\ U^2 + fLU + gh &= 0 \end{aligned} \quad (\text{B.19})$$

possible balances: cyclone

$$\operatorname{sgn}(F_c) = \operatorname{sgn}(F_p):$$

$$U_{1,2} = -fL/2 \pm \sqrt{f^2 L^2 / 4 + gh} \quad (\text{B.20})$$

anti-cyclone

$$\operatorname{sgn}(F_c) = -\operatorname{sgn}(F_p):$$

$$U_{1,2} = -fL/2 \pm \sqrt{f^2 L^2 / 4 - gh} \quad (\text{B.21})$$

$$\begin{aligned} 4gh &\leq f^2 L^2 \\ 2c &\leq fL \\ 2L_R &\leq L \end{aligned} \quad (\text{B.22})$$

#### Derivation 7: Okubo-Weiss-Parameter

**TODO!:!**

$$\begin{aligned} O_w &= \operatorname{Tr} T^2 = \left( \frac{\partial u_i}{\partial x_k} \frac{\partial u_k}{\partial x_j} \hat{e}_i \hat{e}_j \right)_{i,i} \\ &= \frac{\partial u_i}{\partial x_j} \frac{\partial u_j}{\partial x_i} \\ &= \left( \frac{\partial u_i}{\partial x_i} \right)^2 + (1 - \delta_{i,j}) \frac{\partial u_j}{\partial x_i} \frac{\partial u_i}{\partial x_j} \\ &= \left( \frac{\partial u_i}{\partial x_i} \right)^2 + \frac{1}{2} \left( \frac{\partial u_i}{\partial x_j} + \frac{\partial u_j}{\partial x_i} \right)^2 - \frac{1}{2} \left( \frac{\partial u_i}{\partial x_j} - \frac{\partial u_j}{\partial x_i} \right)^2 \\ &= \frac{1}{2} \left( \frac{\partial u_i}{\partial x_i} + \frac{\partial u_j}{\partial x_j} \right)^2 + \frac{1}{2} \left( \frac{\partial u_i}{\partial x_i} - \frac{\partial u_j}{\partial x_j} \right)^2 + \frac{1}{2} \left( \frac{\partial u_i}{\partial x_j} + \frac{\partial u_j}{\partial x_i} \right)^2 - \\ &= \text{divergence}^2 + \text{stretching}^2 + \text{shear}^2 - \text{vorticity}^2 \end{aligned} \quad (\text{B.23})$$

Hence for motion dominated by deformation and shear the system has hyperbolic character, whereas vorticity-dominated motion has parabolic character. Of interest should therefore not only be the value of  $O_w$  but also its gradient. An abrupt change in  $O_w$  clearly identifies regions of vorticity genesis and decay.

In 2 dimensions:

$$O_w = \left( \frac{\partial u}{\partial x} \right)^2 + 2 \frac{\partial u}{\partial y} \frac{\partial v}{\partial x} \quad (B.24)$$

### Derivation 8: Cushman's Drift Speed

$$\begin{aligned} X_t &= -\frac{\beta g'}{f_0^2} \frac{\int H\eta + \eta^2/2 dA}{\int \eta dA} \\ &= -\frac{\beta g'}{f_0^2} \left( H + \frac{\int \eta^2/2 dA}{V_e} \right) \\ &= -\frac{\beta c^2}{f_0^2} \left( 1 + \frac{1}{H} \frac{\int \eta^2/2 dA}{V_e} \right) \\ &= -\beta L_R^2 \left( 1 + \frac{1}{H} \frac{\int \eta^2 dA}{2V_e} \right) \\ &= \frac{\omega_{long}}{k} \left( 1 + \frac{1}{H} \frac{\int \eta^2 dA}{2V_e} \right) \end{aligned} \quad (B.25)$$

### Derivation 9: Mean Fields of $u$ and $b$

**TODO:?**

### Derivation 10: Turbulent Kinetic Energy

diffusion term very small  
on macro scale?

Multiplication of equation (??) with  $u'_i$  over all  $i$  yields

$$\begin{aligned} u'_i \frac{\partial (\bar{u}_i + u'_i)}{\partial t} + u'_i (\bar{u}_j + u'_j) \frac{\partial (\bar{u}_i + u'_i)}{\partial x_j} + u'_i \delta_{j3} \epsilon_{jki} f_j (\bar{u} + u')_k \\ = -u'_i \frac{\partial (\bar{p} + p')} {\partial x_i} + u'_i \nu \frac{\partial^2 (\bar{u}_i + u'_i)}{\partial x_i^2} - u'_i \delta_{3j} \bar{g} \\ \frac{1}{2} \frac{\partial u'^2}{\partial t} + \frac{1}{2} \bar{u}_j \frac{\partial u'^2}{\partial x_j} + u'_i \bar{u}_j \frac{\partial \bar{u}_i}{\partial x_j} + u'_i u'_j \frac{\partial \bar{u}_i}{\partial x_j} + \frac{1}{2} u'_j \frac{\partial u'^2}{\partial x_j} \\ = -u'_i \frac{\partial \bar{p}}{\partial x_i} - u'_i \frac{\partial p'}{\partial x_i} + u'_i \nu \frac{\partial^2 \bar{u}_i}{\partial x_i^2} + \frac{1}{2} \nu \frac{\partial^2 u'^2}{\partial x_j^2} - \nu \left( \frac{\partial u'_i}{\partial x_j} \right)^2 - u'_i \delta_{3j} g \end{aligned} \quad (B.26)$$

First and last term on RHS are again hydrostaticity

$$\begin{aligned} \frac{1}{2} \frac{\partial u'^2}{\partial t} + \frac{1}{2} \bar{u}_j \frac{\partial u'^2}{\partial x_j} + u'_i \bar{u}_j \frac{\partial \bar{u}_i}{\partial x_j} + u'_i u'_j \frac{\partial \bar{u}_i}{\partial x_j} + \frac{1}{2} u'_j \frac{\partial u'^2}{\partial x_j} \\ = -u'_i \frac{\partial p'}{\partial x_i} + u'_i \nu \frac{\partial^2 \bar{u}_i}{\partial x_i^2} + \frac{1}{2} \nu \frac{\partial^2 u'^2}{\partial x_j^2} - \nu \left( \frac{\partial u'_i}{\partial x_j} \right)^2 \end{aligned} \quad (B.27)$$

averaging...

$$\frac{\partial E_t}{\partial t} + \bar{u}_j \frac{\partial E_t}{\partial x_j} - \nu \frac{\partial^2 E_t}{\partial x_j^2} = -\overline{u'_i u'_j \frac{\partial \bar{u}_i}{\partial x_j}} - \overline{u'_i u'_j \frac{\partial \bar{u}_i}{\partial x_j}} - \frac{1}{2} \overline{u'_j \frac{\partial u'^2}{\partial x_j}} - \overline{u'_i \frac{\partial p'}{\partial x_i}} + \nu u'_i \quad (\text{B.28})$$

...

$$\frac{\partial E_t}{\partial t} + \bar{u}_j \frac{\partial E_t}{\partial x_j} = \frac{\partial}{\partial x_j} \left( \nu \frac{\partial E_t}{\partial x_j} + \bar{u}'_j p' + \frac{1}{2} \overline{u'_j u'_i u'_i} \right) - \overline{u'_j u'_i \frac{\partial \bar{u}_i}{\partial x_j}} + \bar{b}' w' - \nu \left( \frac{\partial}{\partial x_j} \right)^2 \quad (\text{B.29})$$

...

$$\frac{\partial E_t}{\partial t} + \bar{u}_j \frac{\partial E_t}{\partial x_j} = \frac{\partial \psi_i}{\partial x_j} - \overline{u'_j u'_i \frac{\partial \bar{u}_i}{\partial x_j}} + \bar{b}' w' - \nu \left( \frac{\partial u'^2}{\partial x_j} \right) \quad (\text{B.30})$$

... with  $\psi = \nu \nabla E_t + \overline{u' p'} + \frac{1}{2} \overline{u' u'^2}$  as the total flux of turbulent kinetic energy.

Invoking again horizontal homogeneity as was done for equation (??), equation (B.30) takes the form

$$\frac{\partial E_t}{\partial t} + \bar{w} \frac{\partial E_t}{\partial z} = \frac{\partial \psi}{\partial z} - \overline{u'_h w' \frac{\partial \bar{u}_h}{\partial z}} + \bar{b}' w' - \nu \overline{(\nabla u')^2} \quad (\text{B.31})$$

derivation still incomplete..  
i assume  $\bar{a} \bar{b}' = \bar{a} \bar{b}$  might help..?



## *Declaration of Authorship*

I, Nikolaus KOOPMANN, declare that this thesis titled, 'Automated Analysis of Meso-Scale Ocean-Eddies from Model Data' and the work presented in it are my own. I confirm that:

- This work was done wholly or mainly while in candidature for a research degree at this University.
- Where any part of this thesis has previously been submitted for a degree or any other qualification at this University or any other institution, this has been clearly stated.
- Where I have consulted the published work of others, this is always clearly attributed.
- Where I have quoted from the work of others, the source is always given. With the exception of such quotations, this thesis is entirely my own work.
- I have acknowledged all main sources of help.
- Where the thesis is based on work done by myself jointly with others, I have made clear exactly what was done by others and what I have contributed myself.

Signed: \_\_\_\_\_

Date: \_\_\_\_\_

sdfhdgfhsgdgbh



# *List of Figures*

- 1.1 Animation snapshot of early test run. Shown is SSH with detected eddies indicated by red and green lines. 13
- 1.2 top: Stommel's equation  $\mathcal{F}_{\text{bottom}} - \mathcal{F}_{\text{surface}} = -v\beta$  with constant eddy viscosity. bottom: Parallel Ocean Program eddy-resolving model snapshot with SSH mean of one year subtracted. 18
- 1.3 Resolutions for model vs satellite. Modified version from [Olbers et al. \(2012\)](#). 22
- 1.4 The ground track patterns for the 10-day repeat orbit of T/P and its successors Jason-1 and Jason-2 (thick lines) and the 35-day repeat orbit of ERS-1 and its successors ERS-2 and Envisat (thin lines). (a) The ground tracks of the 10-day orbit during a representative 7-day period; (b) The ground tracks of the 35-day orbit during the same representative 7-day period; (c) The combined ground tracks of the 10-day orbit and the 35-day orbit during the 7-day period; and (d) The combined ground tracks of the 10- day orbit and the 35-day orbit during the full 35 days of the 35-day orbit. (sic) [Chelton et al. \(2011\)](#) 22
- 1.5 Length of mission. Numbers are orbit-period in days. 23
- 1.6  $\xi(\phi, \mu)$ . Ny  $\equiv 2$  i.e. the Nyquist frequency. 23
- 2.1 SSH with mean over time subtracted. 27
- 2.2 **TODO:YO!** 29
- 2.3 Left: Fourier-fit of an eddy from POP-SSH-data and the 2nd differential thereof. Right: Theoretical Gauss-Shape built from the resulting standard-deviation i.e.  $\sigma$  and amplitude. 30
- 2.4 Different values of the isoperimetric quotient. 31

- 2.5 Left: The Chelton-method expects to detect eddies at their base and is rather tolerant with respect to the form of found contour. The IQ -method aims more at detecting single round vortices without expecting found contour to be necessarily related to any howsoever-defined outer *edge* of the eddy. 32
- 2.6 Stream function of a meandering jet shedding off a vortex. The line of strongest gradient *i.e.* fastest geostrophic speed later becomes the zero-vorticity-line at a theoretical distance  $\sigma$  from the center (Offset of  $\Psi$  is chosen arbitrarily). 32
- 2.7 Zonal x- and z-normalized cyclone-profiles (early data ~ '13/12). 33
- 2.8 A flat wobbly low-latitude eddy resulting in multiple zero-crossings of its  $\nabla^2$ . The problem is addressed by differentiating the profile's Fourier-Series fit instead. 35
- 2.9 Eddies in the North-Atlantic. Y-axis: latitude. X-axis top: ratio of *radius of circle with equal area to that of found contour* to local Rossby-radius. X-axis bottom: ratio of  $\sigma$  to local Rossby-radius. Color-axis: Isoperimetric Quotient. Size: amplitude. The bottom plot suggests that a ratio of say 4 for  $\sigma/L_R$  should be a reasonable threshold. Same graph for the Southern Ocean looks very different though (not shown here), in that said ratio often exceeds ratios as high as 10 and larger in the far south where  $L_R$  becomes very small. This problem was addressed by prescribing a minimum value  $L_R = 20\text{km}$  for the calculation of the scale-theshold. 35
- 2.10 Among the saved meta-information for each eddy are also the indices describing the ellipse that defines the eddy's allowed locations with respect to the next time-step. 36
- 2.11 Each circle represents one eddy in the new time step. Y-axis: Maximum ratio to closest eddy in old set of either amplitude or  $\sigma$ , where 1 means *identical* and 2 means factor 2 difference. The threshold used for the final runs was 2. X-axis: Ratio of distance to closest eddy from old set divided by  $\delta t$  to local long-Rossby-wave phase-speed. Color-axis: Isoperimetric Quotient. Radius of circles: ratio of  $\sigma$  to local Rossby-radius. All eddies with said ratio larger than 10 are omitted. Note the obvious inverse correlation of scale to IQ, suggesting that all large *eddies* likely represent more than one vortex. 38

**2.12**Basic code structure. The only files that are to be edited are the INPUT files. INPUT.m is independant of the origin of data, whilst the files INPUTaviso.m, INPUTpop.m etc set source-specific parameters. Each of the SXX-steps initially calls initialise.m, which in turn scans all available data, reads in the INPUT data via get\_input.m, corrects for missing data etc and creates DD.mat. The latter is the main meta-data file, which gets updated throughout all steps. All data is built step-by-step along the consecutive SXX-steps (red line). The SXX-steps are the only programs that have to be called (in order) by the user. Missing data is filled automatically in each step (Note that meanSsh.mat should be recalculated if the time span is changed!). 40

3.1	aviso-MI: Baseline-shifted <i>old</i> tracks. Tracks younger than 500days omitted.	41
3.2	aviso-MII: Baseline-shifted <i>old</i> tracks. Tracks younger than 500days omitted.	42
3.3	MI: anti-cyclones ind red. Tracks younger than 1a omitted for clarity.	44
3.4	MII: anti-cyclones ind red. Tracks younger than 1a omitted for clarity.	44
3.5	bla	45
3.6	aviso-MI : Births are in blue and deaths in green. Size of dots scales to age squared. Only showing tracks older than one year.	46
3.7	aviso-MI : Total count of individual eddies per 1 degree square.	46
3.8	aviso-MI : TODO	46
3.9	aviso-MI : TODO	47
3.10	aviso-MI : TODO	47
3.11	bla	48
3.12	aviso-MII: Births are in blue and deaths in green. Size of dots scales to age squared. Only showing tracks older than one year.	48
3.13	aviso-MII: Total count of individual eddies per 1 degree square.	48
3.14	aviso-MII: TODO	49
3.15	aviso-MII: TODO	49
3.16	bla	50
3.17	pop7-MII: Total count of individual eddies per 1 degree square.	50
3.18	pop7-MII: TODO	51
3.19	pop7-MII: TODO	51
3.20	pop2aviso-MII: TODO	52
3.21	pop2aviso-MII: TODO	53

3.22 Left: Zonal-mean drift speed (cyan) fit to Fig 22 of (Chelton *et al.*, 2011) (Background). Right:  $\sigma$  and  $L_e$  fit to Fig. 12 of their paper. Dotted lines are medians instead of means. 1st row: aviso-MII , 2nd row: aviso-MI , 3rd row: pop2avi-MII , 4th row: POP-7day-MII . Note that for the very high latitudes ( $> |60^\circ|$ ) the contrast between model and satellite data is further intensified by the lack of satellite data (see figs. 3.14 and 3.18) in those regions (sea-ice / orbit inclinations). For a depiction without this effect see fig. 4.2. 54

- 4.1 All contours that passed the filtering procedure for one exemplary time-step. Top: aviso-MI . Mid: aviso-MII . Bottom: POP-7day-MII . 55
- 4.2 Differences in zonal mean  $\sigma$  between AVISO/POP and AVISO/downscaled POP. Means/Medians are built zonally over only those  $1^\circ \times 1^\circ$ -bins that feature data in both sets *i.e.* the intersection of lat + ii lon of both sets. 56
- 4.3 Eddy count at one point in time for one fully zonal  $1^\circ$ -bin. Top: aviso-MI . Bottom: aviso-MII . The tropical spectrum is broad yet with strong positive skewness *i.e.* oriented towards smaller scales. In high latitudes the standard deviation is smaller. The MI method yields more large eddies. 56
- 4.4 Ratios of  $\sigma$  to  $L$ (see filter 10) 57
- 4.5 The upper part of a Gaussian profile can appear similar to a quadratic one. 57
- 4.6 TODO 58
- 4.7 **TODO:caption** 58

- A.1 1) 2D turbulence with several sinusoidal and random signals as initial condition, 2) at a later time 3) at a much later time.  
Code from ?. 61

## *List of Tables*

1.1 model vs satellite	22
3.1 Fix parameters for all runs.	42



## Bibliography

- Bjerknes, J., & Holmboe, J. 1944. On the Theory of Cyclones. *J. Atmos. Sci.*
- Chelton, Dudley B., Schlax, Michael G., Samelson, Roger M., & de Szoeke, Roland a. 2007. Global observations of large oceanic eddies. *Geophys. Res. Lett.*, **34**(15), L15606.
- Chelton, Dudley B., Schlax, Michael G., & Samelson, Roger M. 2011. Global observations of nonlinear mesoscale eddies. *Prog. Oceanogr.*, **91**(2), 167–216.
- Cipollini, Paolo, Cromwell, David, Jones, Matthew S, Quartly, Graham D, & Challenor, Peter G. 1997. Concurrent altimeter and infrared observations of Rossby wave propagation near 34°N in the Northeast Atlantic. *Geophys. Res. Lett.*, **24**(8), 889–892.
- Cushman-Roisin, B. 1990. Westward motion of mesoscale eddies. *J. Phys.* ....
- Eden, Carsten, & Greatbatch, Richard J. 2008. Towards a mesoscale eddy closure. *Ocean Model.*, **20**(3), 223–239.
- Flierl, Glenn R. 1984. Rossby wave radiation from a strongly nonlinear warm eddy. *J. Phys. Oceanogr.*, **14**(1), 47–58.
- Forget, Gaël. 2010. Mapping Ocean Observations in a Dynamical Framework: A 2004–06 Ocean Atlas. *J. Phys. Oceanogr.*, **40**(6), 1201–1221.
- Killworth, Peter D., Chelton, Dudley B., & de Szoeke, Roland A. 1997. The Speed of Observed and Theoretical Long Extratropical Planetary Waves. *J. Phys. Oceanogr.*, **27**(9), 1946–1966.

- Le Traon, P-Y, & Minster, J-F. 1993. Sea level variability and semiannual Rossby waves in the South Atlantic subtropical gyre. *J. Geophys. Res. Ocean.*, **98**(C7), 12315–12326.
- Matano, Ricardo P, Schlax, Michael G, & Chelton, Dudley B. 1993. Seasonal variability in the southwestern Atlantic. *J. Geophys. Res. Ocean.*, **98**(C10), 18027–18035.
- Matsuura, Tomonori, & Yamagata, Toshio. 1982. On the evolution of nonlinear planetary eddies larger than the radius of deformation. *J. Phys. Oceanogr.*, **12**(5), 440–456.
- Nof, Doron. 1981. On the  $\beta$ -induced movement of isolated baroclinic eddies. *J. Phys. Oceanogr.*, **11**(12), 1662–1672.
- Oestreicher, Samantha. Underwater Mathematics : Illuminating Deep-Reaching Ocean Eddies in Climate Models.
- Okubo, Akira. 1970. Horizontal dispersion of floatable particles in the vicinity of velocity singularities such as convergences. *Deep sea Res. Oceanogr. Abstr.*, **17**(143), 445–454.
- Olbers, Dirk, Willebrand, Jürgen, & Eden, Carsten. 2012. *Ocean Dynamics*. Springer.
- Orbach, Michael K, & Munk, Walter. 2002. THE U . S . COM-MISSION ON OCEAN POLICY. *Natl. Acad. Sci. Washington, DC*, **15**(April), 135–141.
- Rhines, Peter B. 1974. Waves and turbulence on a beta-plane. *J. Fluid Mech.*, **69**(03), 417.
- Rhines, Peter B, & Holland, William R. 1979. A theoretical discussion of eddy-driven mean flows. *Dyn. Atmos. Ocean.*, **3**(2), 289–325.
- Smith, K. Shafer, & Marshall, John. 2009. Evidence for Enhanced Eddy Mixing at Middepth in the Southern Ocean. *J. Phys. Oceanogr.*, **39**(1), 50–69.
- van Leeuwen, Peter Jan. 2007. The Propagation Mechanism of a Vortex on the  $\beta$  Plane. *J. Phys. Oceanogr.*, **37**(9), 2316–2330.